

Demonstrating Quantum Speed-Up with a Two-Transmon Quantum Processor.

Andreas Dewes

May 16, 2012

Contents

1	Introduction & Summary	11
1.1	Quantum Computing & Circuit Quantum Electrodynamics	11
1.2	Realizing a Two-Qubit Quantum Processor	14
1.3	Demonstrating Simultaneous Single-Shot Readout	15
1.4	Generating and Characterizing Entanglement	16
1.5	Realizing a Universal Two-Qubit Quantum Gate	19
1.6	Running a Quantum Search Algorithm	20
1.7	Demonstrating Quantum Speed-Up	21
1.8	Designing a Scalable Quantum Computing Architecture	22
2	Theoretical Foundations	25
2.1	Quantum Mechanics & Quantum Computing	25
2.2	Transmon Qubits	25
2.3	Circuit Quantum Electrodynamics	26
2.3.1	Dispersive Limit & Qubit Readout	26
2.4	The Josephson Bifurcation Amplifier	27
3	Realizing a Two-Qubit Processor	29
3.1	Introduction & Motivation	29
3.2	Qubit Design	30
3.3	Readout Design	30
3.4	Processor Fabrication	30
4	Measurement Setup	31
4.1	Sample Holder & PCB	31
4.2	Cryogenic Wiring	32
4.3	Signal Generation & Acquisition	33
4.3.1	Microwave Sideband Mixing	33
4.3.2	Fast Magnetic Flux Pulses	34
4.3.3	Pulse Synchronization	35

5 Measurement Techniques	37
5.1 Qubit Readout	37
5.2 Qubit Manipulation	37
5.3 Decoherence Time Measurement	37
6 Characterizing the Two-Qubit Processor	39
6.1 Qubit & Readout Characterization	39
6.1.1 Qubit Parameters	40
Readout Parameters	40
Qubit Readout, Driving, Relaxation and Dephasing Time	40
6.2 Single-Qubit Operations	42
6.2.1 Estimation of drive errors	43
6.3 Two Qubit Operations	43
6.3.1 Creation of Entanglement	43
6.3.2 Violation of the Bell Inequality	43
6.3.3 Quantum State Tomography of Two-Qubit States	45
Maximum Likelihood Estimation of Quantum States	45
6.4 Realizing a Two-Qubit Gate	47
6.4.1 Principle	47
6.4.2 Experimental Implementation	47
6.4.3 Quantum Process Tomography of the Gate	47
Introduction & Principle	47
Implementation	47
The Kraus Representation of the Quantum Process	51
6.4.4 Gate Fidelity	52
6.4.5 Gate Error Analysis	52
7 Running the Grover Search Algorithm	55
7.1 Introduction & Motivation	55
7.1.1 Deriving the Grover Algorithm	57
7.1.2 Ancilla-based Implementation of the Algorithm	60
7.2 Comparision to a Classical Algorithm	62
7.3 Experimental Implementation	62
7.3.1 Pulse Sequence	63
7.4 Results	63
7.4.1 State Tomography of the Algorithm	64
7.4.2 Single Run Results	64
7.5 Algorithm Fidelity	66
7.6 Error Analysis	67

CONTENTS	5
-----------------	---

7.6.1 Gate Errors & Decoherence	67
Decoherence	67
Fidelity of the Oracle and diffusion operators	71
7.6.2 Readout Errors	71
7.7 Conclusions	72
8 Designing a Scalable Architecture for Quantum Bits	75
8.1 Definition & Requirements	76
8.2 Qubit Design	76
8.2.1 Qubit Parameters	76
8.2.2 Qubit-Qubit Coupling	76
8.3 Readout Design	76
8.3.1 Readout Parameters	76
8.3.2 Qubit-Readout Coupling	76
8.4 Single-Qubit Manipulation	76
8.4.1 Error Analysis	76
8.5 Multi-Qubit Manipulation	76
8.5.1 Error Analysis	76
8.6 Implementing a Universal Set of Quantum Gates	76
8.7 Realizing A Four-Qubit Architecture	76
8.8 Scaling Up	76
9 Conclusions & Perspective	77
9.1 Future Directions in Superconducting QC	77
9.1.1 3D Circuit Quantum Electrodynamics	77
9.1.2 Hybrid Quantum Systems	77
9.1.3 Quantum Error Correction & Feedback	77
A Modeling of Multi-Qubit Systems	79
A.1 Analytical Approach	79
A.1.1 Multi-Qubit Hamiltonian	79
A.1.2 Energies and Eigenstates	79
A.2 Master Equation Approach	79
A.2.1 Direct Integration	79
A.2.2 Monte Carlo Simulation	79
A.2.3 Speeding Up Simulations	79
B Data Acquisition & Management	81
B.1 Data Acquisition Infrastructure	81
B.2 Data Management Requirements	81

B.3 PyView	81
B.3.1 Overview	81
B.3.2 Instrument Management	81
B.3.3 Data Acquisition	81
B.3.4 Data Management	81
B.3.5 Data Analysis	81
C Design & Fabrication	83
C.1 Mask Design	83
C.2 Optical Lithography	83
C.3 Electron Beam Lithography	83
D Bibliography	83

List of Figures

1.1 Blueprint of a “canonical” two-qubit quantum processor	11
1.2 Circuit schematic of the realized two-qubit processor	14
1.3 Switching probabilities of the two qubit readouts as a function of the readout excitation power	15
1.4 Generating entangled two-qubit states by swapping interaction	17
1.5 Measurement of the CHSH operator of an entangled two-qubit state	18
1.6 Measured χ -matrix of the $\sqrt{i\text{SWAP}}$ gate	19
1.7 Schematic of the implementation of the Grover search algorithm	20
1.8 Measured density matrices when running the Grover algorithm	21
1.9 Single-run results of the Grover search algorithm	21
1.10 Schematic of the multi-qubit architecture realized in this thesis	23
3.1 Circuit schematic of the two-qubit processor	29
4.1 The measurement setup used for the two-qubit experiments	32
6.1 Spectroscopy of the Two-Qubit Processor	39
6.2 A qubit parameter survey showing T_1 , readout contrast and Rabi frequency of the two qubits over a large range of qubit frequencies	41
6.3 Demonstration of single-qubit IQ control	42
6.4	43
6.5 Experimentally created $ \psi_+\rangle$ ($F = 0.91$) and $ \psi_-\rangle$ ($F = 0.93$) states	44
6.6	44
6.7 test	47
6.8 The input-output density matrix of the quantum process tomography of the $\sqrt{i\text{SWAP}}$ gate. Shown are the measured density matrices of 16 different input states and the corresponding output matrices with their state fidelities. The ideal matrices are overlaid in red.	48

6.9	The input-output density matrix of the quantum process tomography of the $\sqrt{i\text{SWAP}}$ gate. Shown are the measured density matrices of 16 different input states and the corresponding output matrices with their state fidelities. The ideal matrices are overlaid in red.	49
6.10	54
7.1	A wavefunction $\psi(x)$ and potential $V(x)$ defined on a grid of points x_1, \dots, x_N	58
7.2	Implementations of the four possible Oracle functions used in the Grover search algorithm, using only reversible gate operations	60
7.3	Full version of an implementation of the two-qubit Grover search algorithm	61
7.4	Classical reversible implementation of a search algorithm on a two-bit input register. The Oracle function can be implemented by two single-bit NOT operations and a Toffoli gate. R designates the generation of a random binary value at the beginning of the algorithm If the Oracle does not yield the correct answer, the test state gets incremented. The average success probability of the algorithm is 50 %.	62
7.5	Schematic of our implementation of the Grover search algorithm	63
7.6	Pulse sequence used for implementing Grovers search algorithm	64
7.7	Quantum state tomographies at different steps during the Grover search algorithm and single-run outcome probabilities	65
7.8	Single-run success probabilities of the Grover search algorithm	66
7.9	Error model used for analyzing gate and decoherence errors for the Grover search algorithm	68
7.10	Quantum state tomographies at different steps during the Grover search algorithm and single-run outcome probabilities	70
7.11	Measured single- and two-qubit readout matrices and crosstalk matrix for the Grover search algorithm experiment	72

List of Tables

7.1	Conditional probabilities $p_{ab/ uv\rangle}$ and statistical fidelities f_{ab} for all possible outcomes ab , measured for our version of Grover's algorithm.	66
7.2	Fitted gate error parameters of the Grover algorithm	69
7.3	Measured fidelities of the quantum Oracle and diffusion operators used in the Grover search algorithm	71

Chapter 1

Introduction & Summary

1.1 Quantum Computing & Circuit Quantum Electrodynamics

This thesis presents experiments performed with a superconducting two-qubit quantum processor. The main goal of this work was to demonstrate a possible quantum computing architecture based on superconducting qubits that follows the canonical blueprint of a quantum processor as shown in fig. 1.1, in accordance with the five criteria formulated by DiVincenzo (2000). By this definition, a universal quantum computer is a register of well-defined quantum bits (1) with long coherence times (2) on which one can perform universal single- and two-qubit quantum gates(3), read out the state of each qubit individually and with high fidelity (4) and reset the qubit register to a well-defined state (5).

Implementing this allegedly simple list of requirements in a system of superconducting qubits has been a major research challenge during the last decade. Incoherent quantum tunneling in a superconducting device was observed for the first time by Devoret et al. (1985); Martinis et al. (1985) and Clarke et al. (1988), which showed that it

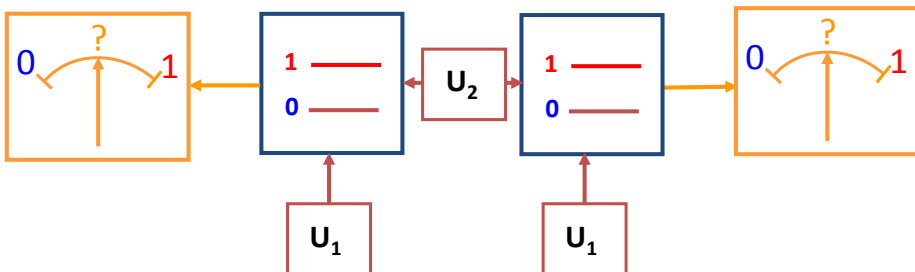


Figure 1.1: The blueprint of a “canonical” two-qubit quantum processor. Shown are two qubits that can be individually manipulated (U_1) and are connected by a universal two-qubit gate U_2 . Each of the qubits can be read out individually.

is possible to cool down a Josephson junction sufficiently to see quantum-mechanical tunneling between different quantum levels of the system. However, the observation of incoherent quantum tunneling did not prove that the quantum state of these devices could be manipulated coherently. The first demonstration of such coherent quantum behaviour in a superconducting system was achieved more than ten years later by Nakamura et al. (1999), who measured for the first time coherent energy oscillations between two quantum levels of a Cooper pair box. This experiment created a large interest in superconducting quantum circuits and led to development of a research field on superconducting quantum computing. In the years after Nakamuras experiment, several types of superconducting qubits were proposed using Josephson junctions in different configurations to realize systems where e.g. the Josephson phase (Martinis et al., 2002) or the magnetic flux inside a superconducting ring (Mooij et al., 1999; Chiorescu et al., 2003) are the dominant quantum variables. In this context, an important result on the way to robust superconducting qubits was the development of the so-called *Quantronium* qubit by Vion et al. (2002). The Quantronium is a Cooper pair box with comparable Josephson and charging energies operated at a well-defined “sweet spot” at which the sensitivity of the device to charge and flux noise is greatly reduced. The high coherence times achieved with the Quantronium –values larger than $2 \mu s$ have been reported– allowed for the first time the implementation of NMR-like quantum operations using a superconducting qubit (Collin et al., 2004). Shortly after that, in 2004, the development of another new type of qubit, the so called *Transmon*, by Wallraff et al. (2004) marked again a drastic improvement in coherence times, qubit robustness and usability. The Transmon qubit is a Cooper pair box shunted with a large capacitor that drastically decreases the charging energy of the system and thus renders the device almost insensitive to charge noise, however still leaving sufficient anharmonicity to operate the device as a qubit. With the Transmon, coherence times comparable or higher than those reported for the Quantronium have been achieved *without* operating the qubit at a special working point, thereby greatly reducing experimental complexity. Furthermore, by embedding the Transmon qubit in a superconducting coplanar waveguide (CPW) resonator it is possible to protect it from external sources of electrical noise and use the dispersive interaction between the qubit and the resonator for reading out the qubit state (Blais et al., 2004). This approach of embedding a superconducting qubit in a waveguide resonator has been termed –in analogy with conventional quantum electrodynamics– *circuit quantum electrodynamics* (CQED) and gained wide popularity in the superconducting qubit community **!1!**. So far, using this CQED approach, superconducting quantum processors with up to three qubits have been realized and two- and three-qubit quantum gates (Fedorov et al., 2011), multi-qubit entanglement (DiCarlo et al., 2010) and simple quantum algorithms (DiCarlo et al., 2009) as well as quantum error correction (Reed et al., 2011) have been demonstrated. Futhermore, experiments demonstrating

To Do 1: add some citations of relevant experiments

fundamental quantum effects that before were accessible only in quantum optics have been performed, demonstrating e.g. QND measurements of photons in a cavity (Johnson et al., 2010), the resolution of photon-number states (Schuster et al., 2007) and the measurement of the Autler-Townes and Mollow transitions with a superconducting qubit (Baur et al., 2009).

Recently, a new type of CQED architecture has been developed by Paik et al. (2011) that combines Transmon qubits with 3D cavities instead of CPW resonators, resulting again in an impressive increase of qubit coherence times of up to two orders of magnitude, with reported qubit relaxation times as high as $80 \mu\text{s}$ **!2!** and decoherence times at a comparable time scale. These drastically improved coherence times have already made possible the realization of elemental quantum feedback and error correction schemes with these systems **!3!** and make them promising candidates for the realization of a superconducting quantum computer. **!4!**

To Do 2: verify this!

To Do 3: cite Irfan's paper here

To Do 4: expand this section as soon as new relevant material appears, include recent IBM, Yale

In parallel to this, the development of quantum-limited amplifiers based on nonlinear superconducting resonators by Siddiqi et al. (2004) and Vijay et al. (2009) provided a very useful tool for measuring and amplifying weak quantum signals, which was already used in several context within the field of superconducting qubits: By operating such a nonlinear amplifier in a hysteretic regime and coupling it, in analogy to the CQED approach, dispersively to a superconducting qubit, Siddiqi et al. (2006) and Mallet et al. (2009) were able to demonstrate a high-fidelity readout scheme for Transmon qubits, reaching up to 97 % readout fidelity. Vijay et al. (2011) used quantum-limited amplifiers to read out a Transmon qubit coupled to a linear microwave cavity and were able to observe quantum jumps of its state. **!5!** used a similar setup with a 3D Transmon to implement a quantum feedback scheme to phase-stabilize a Rabi oscillation of a superconducting qubit.

To Do 5: Add Quantum Feedback Paper Here

With the research presented in this thesis we aim **!1!** to complement the CQED architecture as outlined in the last sections by combining a multi-qubit architecture based on Transmon qubits with a readout scheme based on a nonlinear bifurcation amplifier, thus providing the so-far missing per-qubit single-shot readout that is needed to realize a canonical superconducting quantum processor with these devices.

Comment 1: can I really say "we" here or should it be "I"?

The first part of the thesis discusses the realization of a superconducting two-qubit processor based on Transmon qubits fitted with individual single-shot readouts. With this processor, we implement elementary one- and two-qubit quantum operations and use it to run a simple quantum algorithm that demonstrates probabilistic quantum speed-up. Finally, we discuss the realization of a four-qubit quantum processor using a more scalable approach that could possibly be extended to an even larger number of qubits.

1.2 Realizing a Two-Qubit Quantum Processor

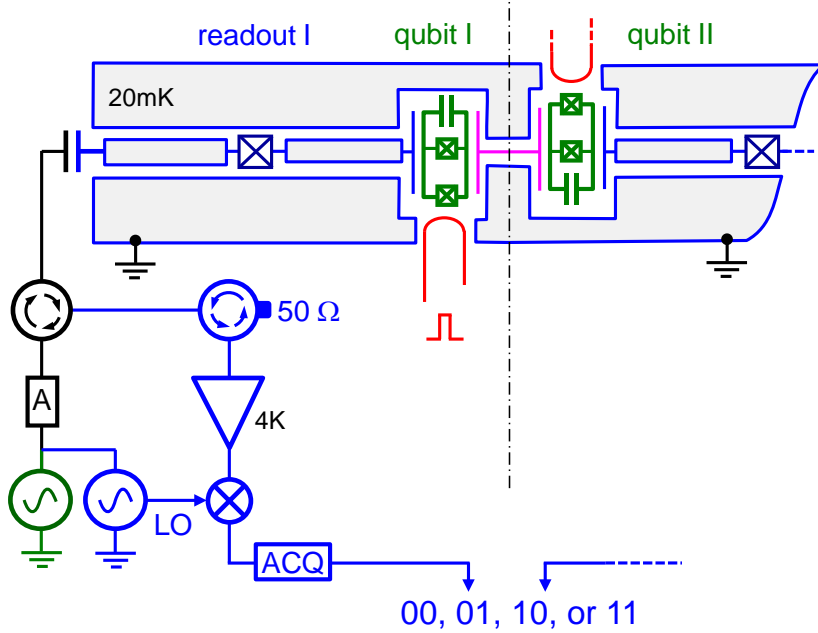


Figure 1.2: Circuit schematic of the two-qubit processor realized in this work, showing the two qubits in green, the qubit readouts in blue and the fast flux lines in red. Each qubit is embedded in its own nonlinear readout resonator and can be driven and read out through an individual microwave line.

The quantum processor implemented in this work is shown in fig. 1.2. It consists of two superconducting quantum bits of the Transmon type, each equipped with its own drive and readout circuit. The qubit readout is realized using a nonlinear coplanar-waveguide resonator that serves as a so-called *cavity bifurcation amplifier* (CBA)(Siddiqi et al., 2006; Mallet et al., 2009; Vijay et al., 2009) and allows a single-shot readout of the qubit state. Each qubit can be manipulated by driving it with microwave pulses through its readout resonator, allowing for robust and fast single-qubit operations. The qubit frequencies can be tuned individually using fast flux lines, allowing us to change the frequency of each qubit over a range of several GHz. The coupling between the two qubits is realized through a fixed capacitance that connects the two top-electrodes of the Transmons and implements a fixed σ_{xx} -type qubit-qubit coupling. This coupling allows us to generate entangled two-qubit states and to implement a two-qubit gate. We use this simple processor to generate entangled two-qubit states, test the Bell inequality, implement an universal two-qubit gate and perform a simple quantum algorithm that demonstrates probabilistic quantum speed-up, as will be discussed in the following sections.

1.3 Demonstrating Simultaneous Single-Shot Readout

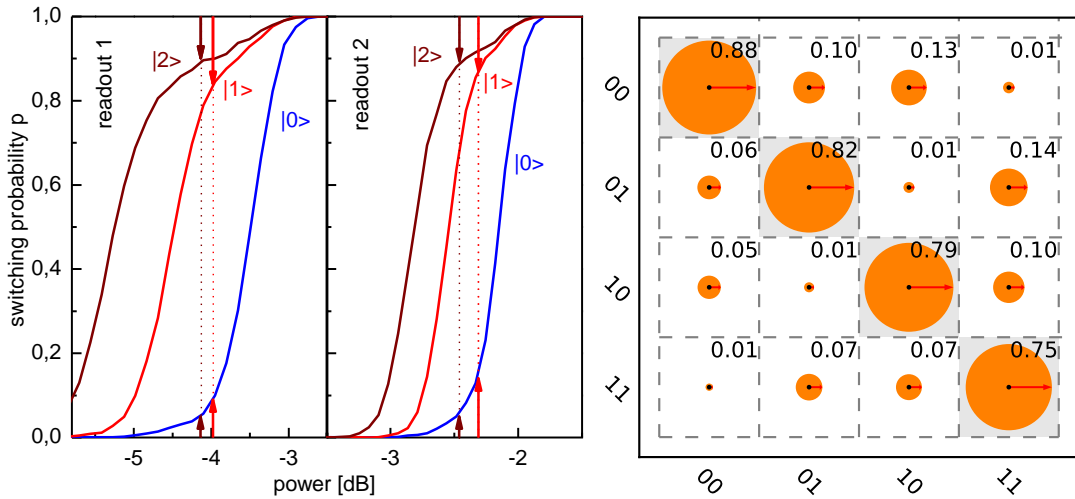


Figure 1.3: a) Switching probabilities of the two qubit readouts as a function of the readout drive power at a fixed driving frequency. The measurement is performed after preparing the qubits in the states $|0\rangle$, $|1\rangle$ and $|2\rangle$. The readout contrast is given as the difference in probability between the curves corresponding to the states $|0\rangle$ and $|1\rangle$ or $|2\rangle$, respectively. The highest contrasts of 88 and 89 % are achieved when the qubit is in state $|2\rangle$. b) Readout matrix of the two-qubit system. The matrix contains the probabilities of obtaining a given measurement result after having prepared the system in a given state. **Figure Comment 2:** Replace this figure since it is not very intuitive. It would be better to show something which allows the reader to directly quantify the visibility and readout crosstalk present in the system.

For the read out the qubit state we use a so called *cavity bifurcation amplifier* (CBA). This approach consists in capacitively coupling the qubit to a coplanar waveguide resonator that is rendered nonlinear by placing a Josephson junction in its center conductor. The capacitive coupling between the qubit and the resonator creates a dispersive interaction between them that induces a change of the resonance frequency of the resonator dependent on the state of the qubit, and vice versa. Furthermore, the resonator can exhibit bistability at certain drive parameters due to its nonlinearity. Therefore, by driving it at a carefully chosen frequency and drive amplitude we can use the dispersive qubit-resonator interaction to map the state of the qubit to one of the bistable states of the resonator. We can then stabilize this resonator state by changing its operating point, effectively freezing it from the further evolution of the qubit state. This allows us to measure the state of the resonator with high precision without being limited by qubit relaxation, thereby providing a high-fidelity, single-shot qubit readout. Contrary to other CQED approaches, in our setup each individual qubit is fitted with such a CBA readout, allowing hence a simultaneous readout of the full two-qubit register, following the canonical blueprint of a quantum computer as formulated by DiVincenzo. For single-qubit CBA

readouts, readout fidelities up to 93 % have been reported (Mallet et al., 2009). However, due to the higher complexity and design constraints of our system, only 83-89 % fidelity have been achieved for the processor presented here. The full characterization of the readout of our processor is shown in fig. 1.3. Fig. 1.3a shows the switching probabilities of each individual qubit readout as a function of the drive amplitude, measured at a fixed drive frequency. Individual curves correspond to the qubit being prepared in different states $|0\rangle$, $|1\rangle$ or $|2\rangle$, the difference between either two curves giving the readout contrast between those qubit states. Preparing the qubit in state $|2\rangle$ before readout can increase the readout fidelity by more than 10 % and is therefore often used in the experiments presented in this thesis. Fig. 1.3b shows the full readout matrix of the two-qubit register that relates measured readout switching probabilities with real qubit state occupation probabilities and allows us to correct readout errors when performing quantum state tomography. In the main text of this thesis we discuss all relevant readout fidelities and errors in details and analyze different error sources limiting the readout performance in our experiments.

1.4 Generating and Characterizing Entanglement

The capacitive coupling between the two qubits provides a σ_{xx} -type interaction that can be used to generate entangled two-qubit states. Conveniently, this coupling is only effective when the qubit frequencies are near-resonant and can therefore be effectively switched on and off by tuning the qubit frequencies in and out of resonance. For the processor realized in this work, the effective coupling constant g of the two qubits has been measured as $2g = 8.2$ MHz. When the two qubits are in resonance, the effective Hamiltonian of the two-qubit system can be written as

$$U(t) = \begin{pmatrix} 1 & 0 & 0 & 0 \\ 0 & \cos 2\pi t g & i \sin 2\pi t g & 0 \\ 0 & i \sin 2\pi t g & \cos 2\pi t g & 0 \\ 0 & 0 & 0 & 1 \end{pmatrix} \quad (1.1)$$

, where $U(t)$ is written in the basis $\{|00\rangle, |01\rangle, |10\rangle, |11\rangle\}$. By using fast flux pulses to non-adiabatically tune the qubits in and out of resonance we can switch on this interaction for a well-defined time. We first characterize the effect of the coupling on the qubit register by preparing the state $|10\rangle$, tuning the qubits in resonance for a given time and measuring the qubit state afterwards. The resulting curve is shown in fig. 1.4 and clearly shows energy oscillations between the two qubits. Analyzing this curve allows us to extract the effective coupling strength between the qubits. Leaving the interaction between the qubits on for a well-defined time allows us to generate entangled Bell states that we

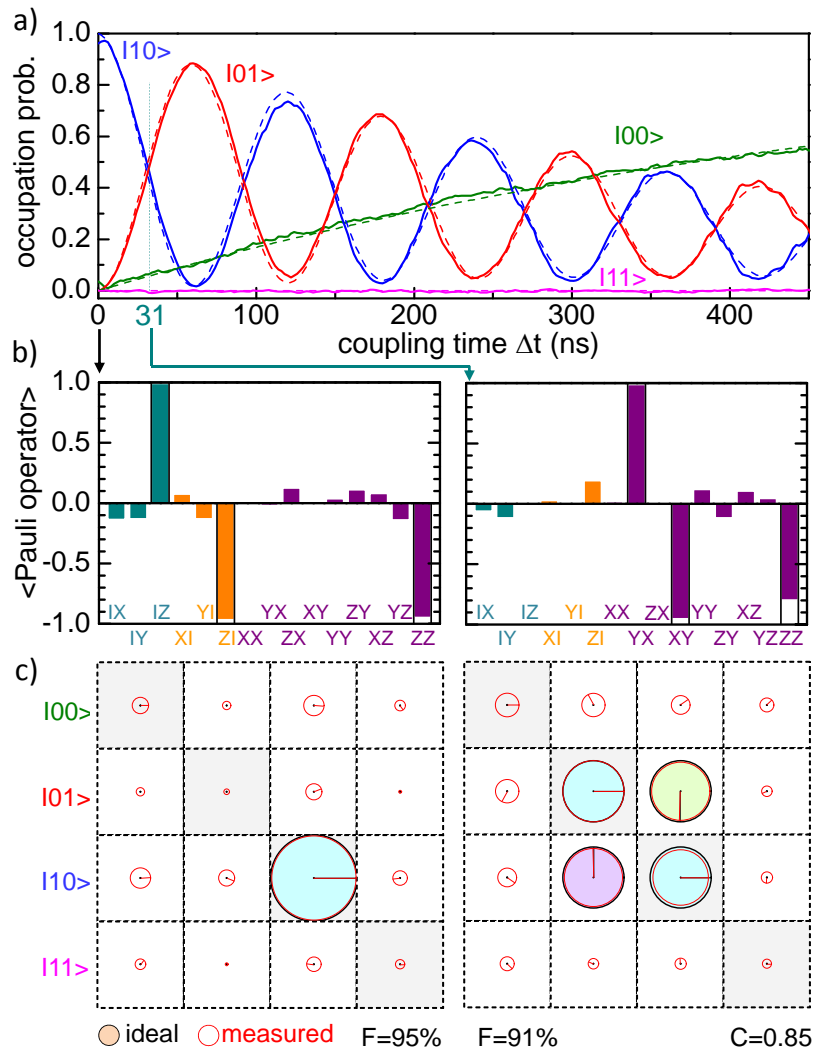


Figure 1.4: Energy oscillations between the two qubits induced by a resonant swapping interaction between them. a) The qubit state after switching on the swapping interaction for a given time Δt . The frequency of the oscillations corresponds to $2g = 8.7$ MHz. b) The Pauli set of the two-qubit state measured at 0 ns and 31 ns. c) The reconstructed density matrices corresponding to the two measured Pauli sets. In c), the area of each circle corresponds to the absolute value of each matrix element and the color and direction of the arrow give the phase of each element. The black circles correspond to the density matrices of the ideal states $|10\rangle$ and $1/\sqrt{2}/(|10\rangle + i|01\rangle)$, respectively. **Figure Comment 4: verify sign!**

characterize by performing quantum state tomography. The experimental reconstruction of the density matrix of such a Bell-state of the type $|\psi\rangle = 1/\sqrt{2}(|01\rangle + i|10\rangle)$ is shown in fig. 1.4b. The measured fidelity of the prepared state of 91 % and the concurrence of 85 % confirm that entanglement is present in the system. We also characterize the entanglement between the two qubits by measuring the so-called *Clauser-Horne-Shimony-Holt* operator (Clauser et al., 1969), which combines measurements of the state of the two qubits along different axes on the Bloch sphere and provides a test that can distinguish between classical correlation and quantum entanglement in a two-qubit system.

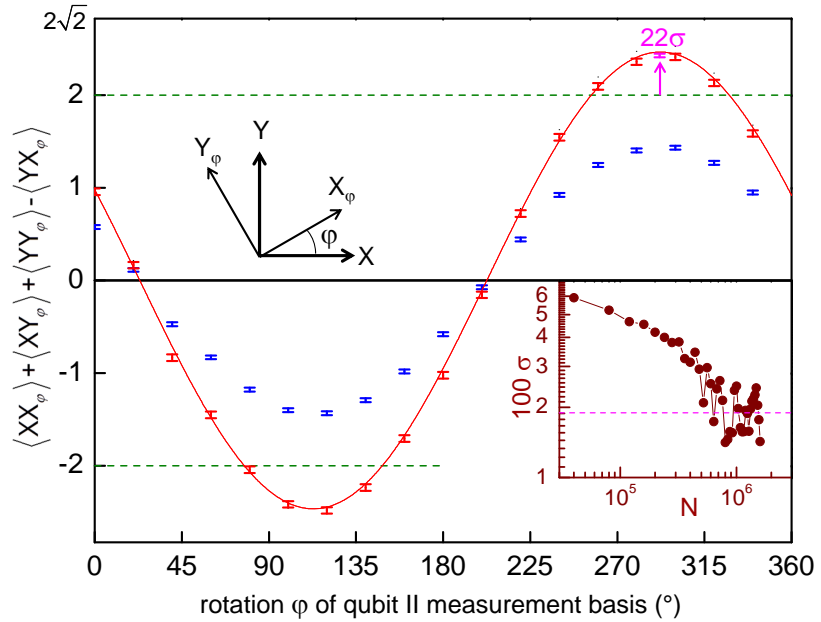


Figure 1.5: Measurement of the CHSH operator for an entangled two-qubit state. The renormalized CHSH expectation value (red points) exceeds the classical boundary of 2 by a large amount. The raw measurement data (blue points) lies below this critical threshold. The inset shows the standard deviation σ at the highest point of the curve as a function of the measurement sample size. For the highest sample count, the classical boundary is exceeded by 22 standard deviations. [Figure Comment 6: p. 140 in cavities 6 labbook](#)

For classical states, the maximum value of the CHSH operator is bound by 2 but for entangled states it can reach a maximum of $2\sqrt{2}$. Fig. 1.5 shows the result of such a CHSH-type measurement performed on a state created by the method described above, showing the value of $\langle \text{CHSH} \rangle$ as a function of the angle ϕ of the measurement basis (more details about the measurement and the preparation of the entangled state can be found in the main text). We observe a violation of the classical boundary 2 of the operator by 22 standard deviations when correcting the readout errors that are present in our system. The raw, uncorrected data fails to exceed the non-classical bound due to readout errors mainly caused by qubit relaxation during the readout. Nevertheless, the observed violation of the equation in the renormalized measurement data is a strong

indication of entanglement in the system.

1.5 Realizing a Universal Two-Qubit Quantum Gate

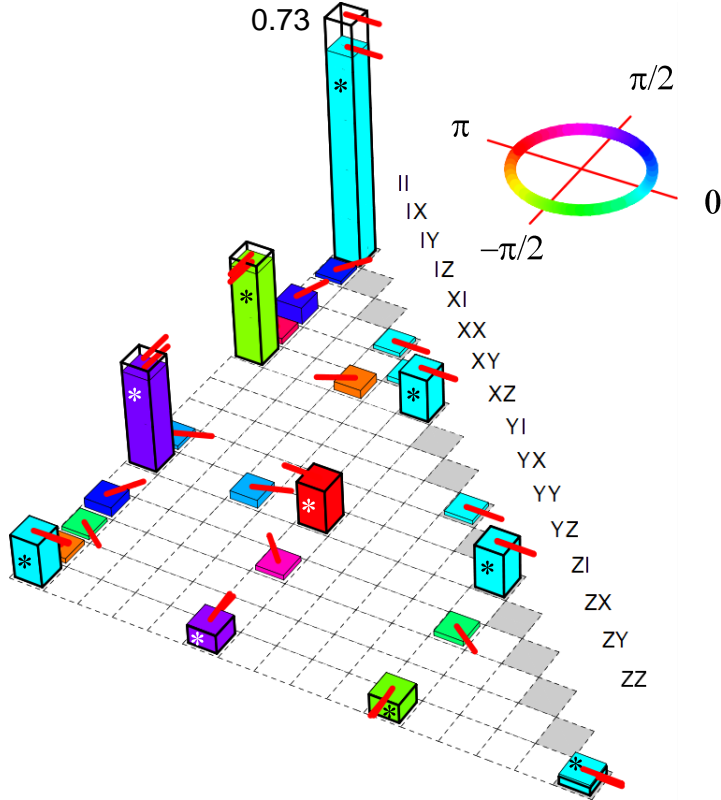


Figure 1.6: The measured χ -matrix of the implemented $\sqrt{i\text{SWAP}}$ gate. The row labels correspond to the indices of the E_i operators, the height of each bar to the absolute value of the corresponding matrix element and the color and direction of the red arrow to the complex phase of each element. The ideal χ -matrix of the $i\sqrt{\text{SWAP}}$ gate is given by the outlined bars. The upper half of the positive-hermitian matrix is not shown.

The swapping evolution given by eq. (1.1) allows not only the preparation of entangled two-qubit states but also the implementation of a two-qubit gate. When switching on the interaction for a time $t_{\pi/2} = 1/8g$ we can realize the so-called $\sqrt{i\text{SWAP}}$ gate, which has the representation

$$U(t) = \begin{pmatrix} 1 & 0 & 0 & 0 \\ 0 & 1/\sqrt{2} & i\sqrt{2} & 0 \\ 0 & i\sqrt{2} & 1/\sqrt{2} & 0 \\ 0 & 0 & 0 & 1 \end{pmatrix} \quad (1.2)$$

and is a universal two-qubit quantum gate. We characterize the operation and errors of our implementation of this gate by performing quantum process tomography, obtaining a gate fidelity of 90 %. The 10 % error in gate fidelity is caused mainly by qubit relaxation and dephasing during the gate operation and only marginally by deterministic preparation errors, as will be discussed in the main text of the thesis. Fig. 1.6 show the measured χ matrix of the gate, which contains the full information on the unitary and

non-unitary action of the gate. The achieved fidelity of the gate operation is sufficient to allow the implementation of a simple quantum algorithm with our processor, as will be discussed in the following section.

1.6 Running a Quantum Search Algorithm

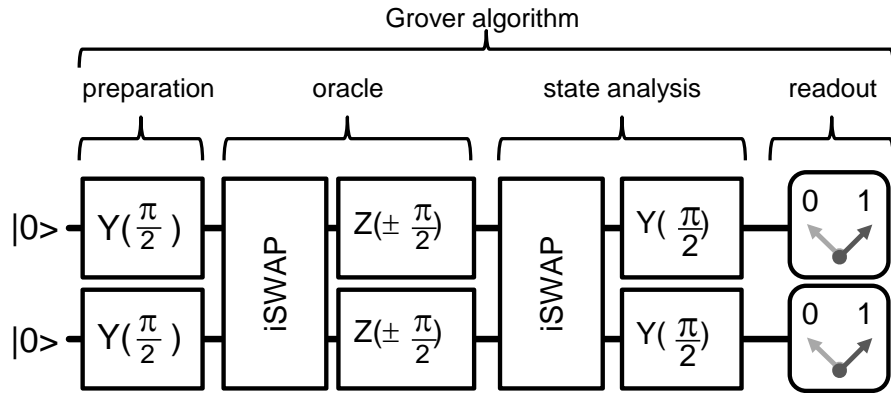


Figure 1.7: Schematic of the implementation of the Grover search algorithm on our two-qubit quantum processor. The algorithm consists in preparing a fully superposed state, applying the quantum Oracle operator to this state and analyzing the resulting output to determine the operator that has been applied with only a single call to the Oracle function.

We can use a two-qubit quantum gate derived from the one described above to run a simple quantum algorithm on our processor, the so called *Grover search algorithm* (Grover, 1997). The version of this algorithm that we implemented operates on a two-qubit basis $x_i \in \{ |00\rangle, |01\rangle, |10\rangle, |11\rangle \}$ and can distinguish between four different *Oracle functions* $f(x)$ with $x \in x_i$ that each tag one given basis state x_j . In the two-qubit case, this algorithm requires only one evaluation of the Oracle function $f(x)$ to determine which state has been marked by the Oracle operator and is therefore faster than any classical algorithm, which would need at most three evaluations of the Oracle function to determine it with certainty. Therefore, it demonstrates the concept of quantum speed-up in a straightforward and intuitive way. The schematic of our version of the Grover algorithm is shown in fig. 1.7 and involves two *iSWAP* gate operations and six single-qubit operations along with a single-shot qubit readout at the end of the algorithm. We implemented this algorithm with our two-qubit processor and performed quantum state tomography after each step to reconstruct the quantum state at different points in the algorithm.

Fig. 1.8 shows the experimentally measured density matrices when running this algorithm with an Oracle operator that marks the state $|00\rangle$. State tomographies are shown after applying a generalized Hadamard transform to the initial state $|00\rangle$, after

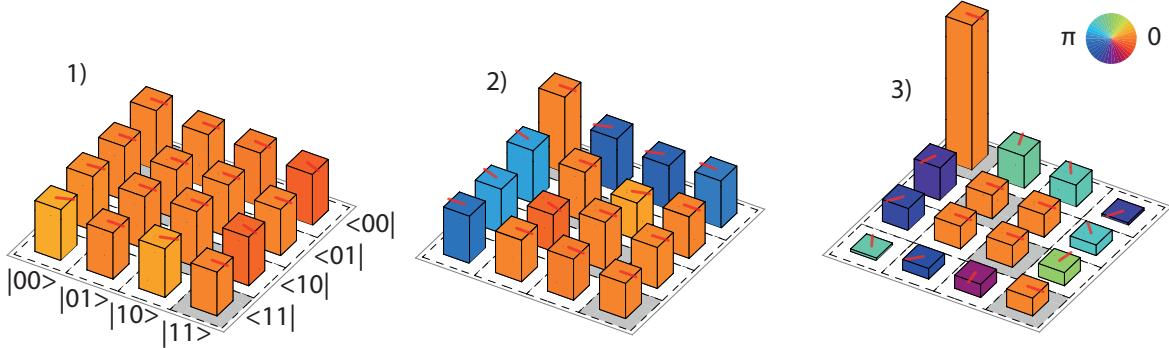


Figure 1.8: Measured density matrices when running the Grover search algorithm with a search oracle marking the state $|00\rangle$. 1) shows the state after the generalized Hadamard transform, 2) after applying the quantum oracle and 3) after the final step of the algorithm.

evaluating the quantum Oracle function and after the final step of the algorithm. The measured state tomographies after the final state of the algorithm yield state fidelities of 68%, 61%, 64% and 65% for the four different Oracle functions, respectively. These fidelities have been corrected for readout errors and therefore do not quantify the quantum speed-up that can be achieved when running this algorithm with our processor. For this it is necessary to analyze the uncorrected single-shot readout outcomes, which we will do in the next section, showing that it is possible to demonstrate a form of probabilistic quantum speed-up with our processor.

1.7 Demonstrating Quantum Speed-Up

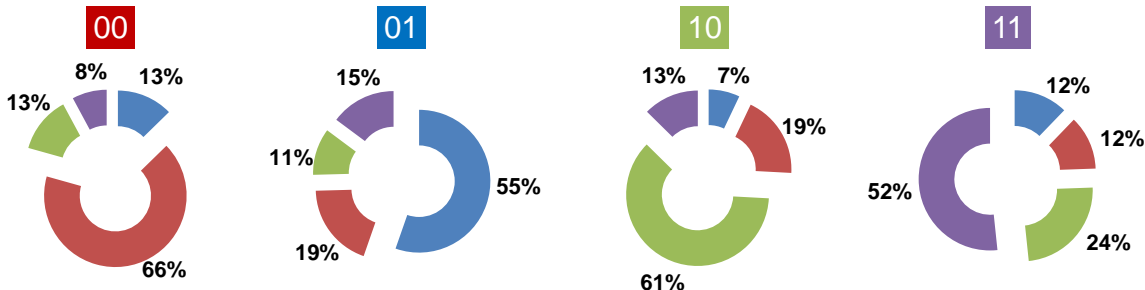


Figure 1.9: Single-run results when running the Grover search algorithm on our two-qubit quantum processor. Shown are the probabilities of obtaining the results 00, 01, 10, 11 as a function of the Oracle function provided to the algorithm, indicated by the number on top of each graph. In all four cases, the success probability of the algorithm is $> 50\%$, thus outperforming any classical query-and-guess algorithm in the required number of calls to the Oracle function.

The main interest of running a quantum algorithm is to obtain an advantage in the run-time in comparison to a classical algorithm, the so-called *quantum speed-up*. To

characterize this quantum speed-up as obtained with our processor, we run the Grover algorithm for all four possible Oracle functions and directly read out the state of the qubit register after the last step of the algorithm instead of performing quantum state tomography, thus not correcting any readout errors. By averaging the outcomes of many such individual runs of the algorithm with different Oracle functions we obtain the so-called *single-run fidelities*, which –for the four different Oracle functions– have been measured as 66%, 55%, 61% and 52%. The full probability distributions for the four possible cases and are shown in fig. 1.9. The measured success probabilities that are $> 50\%$ demonstrate the probabilistic quantum speed-up achieved with our processor compared to a classical query-and-guess algorithm that would be able to give the correct answer with only 50% single-run fidelity (a detailed explanation of this value can be found in the section on the Grover search algorithm in the main part of this thesis). The achieved success probabilities still are considerably lower than the theoretically possible values of 100 % , where the errors are mainly due to relaxation and decoherence of the qubit state during the runtime of the algorithm and to a small degree also due to errors in the pulse sequence.

1.8 Designing a Scalable Quantum Computing Architecture

!2!

Comment 2: this section is still quite incomplete and now well-written, I have to work on the section on scalable architectures to get some more ideas

After having demonstrated the different building blocks of a Transmon-based quantum processor it remains to be shown that larger-scale quantum-computing beyond two qubits is possible with such systems. In this work we therefore investigate the realization of a more scalable qubit architecture using up to six qubits of the Transmon type. Within this approach, we equip each individual Transmon with a single-shot bifurcation readout and drive the whole qubit register and all readout resonators through a multiplexed drive and readout circuit. Qubit-qubit coupling is mediated through a high-Q CPW resonator that acts as a so-called *quantum bus* (Majer et al., 2007). As before, each qubit possesses a fluxline for fast frequency control. To demonstrate the viability of this approach, we realize a four-qubit chip along these lines of design and characterize it experimentally. Preliminary results of these experiments will be discussed in the main text of this thesis, along with the design and implementation of the four-qubit chip in general.

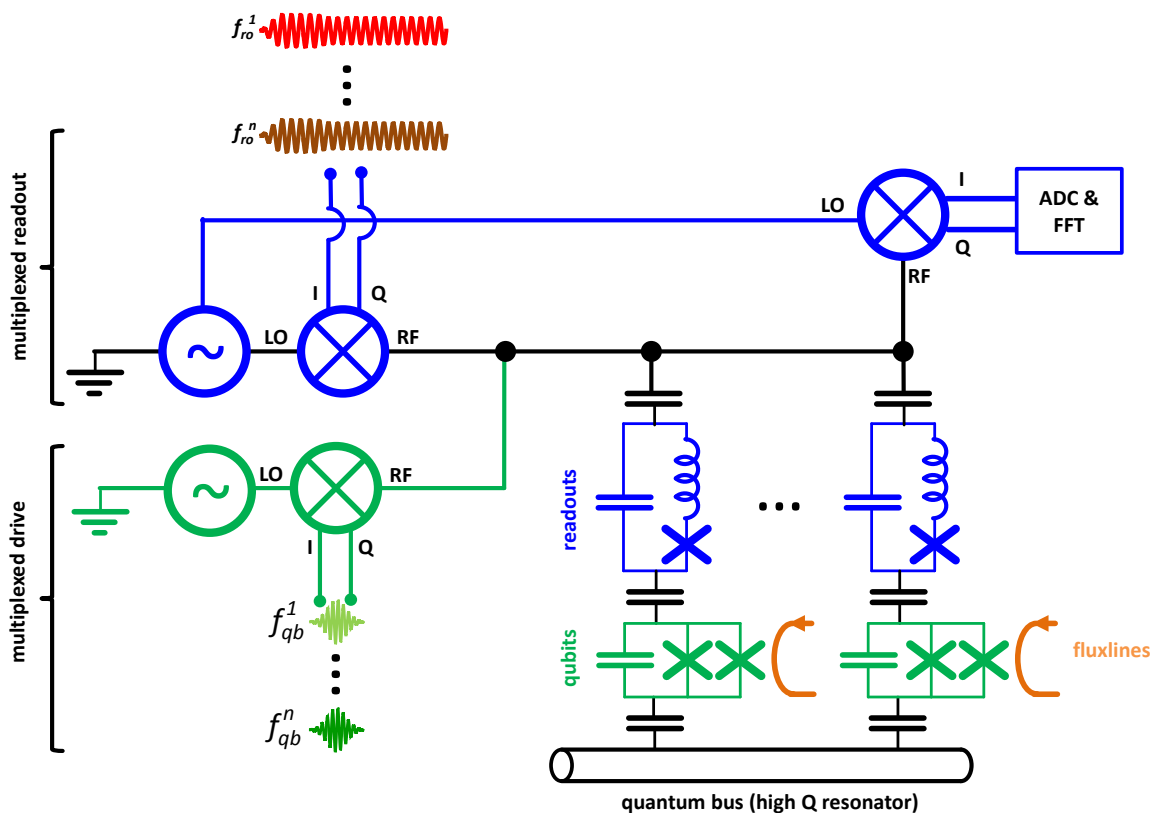


Figure 1.10: A schematic of the multi-qubit architecture realized in this thesis. Qubits and corresponding drive circuits are shown in green, JBA readouts and corresponding drive and measurement circuits in blue. Multiplexed drive and readout lines are used to manipulate and read out the qubits.

Chapter 2

Theoretical Foundations

The goal of this chapter is to provide the theoretical foundations needed to interpret and analyze the experiments discussed in the following chapters. We will therefore briefly introduce some basic concepts of quantum mechanics and quantum computing, discuss Transmon qubits and circuit quantum electrodynamics (CQED) and introduce the reader to the Josephson bifurcation amplifier that we use to read out the qubit state in our experiments. Further details on all the elements discussed here will be provided in the relevant sections of the “Experiments” chapter.

2.1 Quantum Mechanics & Quantum Computing

2.2 Transmon Qubits

A Transmon qubit is essentially a Cooper pair box (CPB) operated in the phase regime, where $E_J \gg E_C$. The Hamiltonian of the CPB can be written as (Cottet, 2002)

$$\hat{H} = 4E_C (\hat{n} - n_g)^2 - E_J \cos \hat{\phi} \quad (2.1)$$

where $E_C = e^2/C_\Sigma$ is the charging energy with $C_\Sigma = C_J + C_B + C_g$ the total gate capacitance of the system, \hat{n} is the number of Cooper pairs transferred between the islands, n_g the gate charge, E_J the Josephson energy of the junction and $\hat{\phi}$ the quantum phase across the junction.

This Hamiltonian can be solved exactly in the phase basis with the solutions being given as (Koch et al., 2007; Cottet, 2002)

$$E_m(n_g) = E_C a_{2[n_g+k(m,n_g)]}(-E_J/E_C) \quad (2.2)$$

Here, $a_\nu(q)$ denotes Mathieu's characteristic value and $k(m, n_g)$ is a function that sorts

the eigenvalues. We'll denote the energy differences between individual eigenstates by $E_{ij} = E_j - E_i$. The absolute anharmonicity of the first two Transmon transitions is given as $\alpha \equiv E_{12} - E_{01}$, the relative anharmonicity as $\alpha_r \equiv \alpha/E_{01}$. In the limit $E_J \gg E_C$ these are well approximated by $\alpha \simeq -E_C$ and $\alpha_r \simeq -(8E_J/E_C)^{-1/2}$.

2.3 Circuit Quantum Electrodynamics

For readout and noise protection, the Transmon qubit is usually coupled to a harmonic oscillator which is usually realized as a lumped-elements resonator or a coplanar waveguide resonator. In the limit where the resonator capacity $C_r \gg C_\Sigma$ we can write the effective Hamiltonian of the system as

$$\hat{H} = \hbar \sum_j \omega_j |j\rangle \langle j| + \hbar \omega_r \hat{a}^\dagger \hat{a} + \hbar \sum_{i,j} g_{ij} |i\rangle \langle j| (\hat{a} + \hat{a}^\dagger) \quad (2.3)$$

Here, $\omega_r = 1/\sqrt{L_r C_r}$ gives the resonator frequency and \hat{a} (\hat{a}^\dagger) are annihilation (creation) operators acting on oscillator states. The voltage of the oscillator is given by $V_{rms}^0 = \sqrt{\hbar \omega_r / 2C_r}$ and the parameter β gives the ratio between the gate capacitance and total capacitance, $\beta = C_g/C_\Sigma$. The coupling energies g_{ij} are given as

$$\hbar g_{ij} = 2\beta e V_{rms}^0 \langle i | \hat{n} | j \rangle = \hbar g_{ji}^* \quad (2.4)$$

When the coupling between the resonator and the Transmon is weak $g_{ij} \ll \omega_r, E_{01}/\hbar$ we can ignore the terms in eq. (2.3) that describe simultaneous excitation or deexcitation of the Transmon and the resonator and obtain a simpler Hamiltonian in the so-called *rotating wave approximation* given as

$$\hat{H} = \hbar \sum_j \omega_j |j\rangle \langle j| + \hbar \omega_r \hat{a}^\dagger \hat{a} + \left(\hbar \sum_i g_{i,i+1} |i\rangle \langle i+1| \hat{a}^\dagger + H.c. \right) \quad (2.5)$$

2.3.1 Dispersive Limit & Qubit Readout

When the qubit frequency is far detuned from the resonator frequency direct qubit-resonator transition get exponentially suppressed and the only interaction left between the two system is a dispersive shift of the transition frequencies. In this limit, the effective Hamiltonian of the system can be written as (Blais et al., 2004; Koch et al., 2007)

$$\hat{H}_{eff} = \frac{\hbar \omega'_{01}}{2} \hat{\sigma}_z + \hbar(\omega'_r + \chi \hat{\sigma}_z) \hat{a}^\dagger \hat{a} \quad (2.6)$$

Here, the resonance frequencies of both the qubit and the resonator are shifted and given as $\omega'_r = \omega_r - \chi_{12}/2$ and $\omega'_{01} = \omega_{01} + \chi_{01}$. The dispersive shift χ itself is given as

$$\chi = \chi_{01} - \chi_{12}/2 \quad (2.7)$$

$$\chi_{ij} = \frac{g_{ij}^2}{\omega_{ij} - \omega_r} = \frac{(2\beta e V_{rms}^0)^2}{\hbar^2 \Delta_i} |\langle i | \hat{n} | i+1 \rangle|^2 \quad (2.8)$$

The fact that χ_{01} and χ_{12} contribute to the total dispersive shift can cause the overall dispersive shift to become negative and even diverge at some particular working points.

2.4 The Josephson Bifurcation Amplifier

(Palacios-Laloy, 2010)

$$[L_e + L_J(i)]\ddot{q} + R_e \dot{q} + \frac{q}{C_e} = V_e \cos(\omega_m t) \quad (2.9)$$

Expanding this to second order in L_J leads to the expression

$$\left(L_e + L_J \left[1 + \frac{\dot{q}^2}{2I_0^2} \right] \right) \ddot{q} + R_e \dot{q} + \frac{q}{C_e} = V_e \cos(\omega_m t) \quad (2.10)$$

Defining the total inductance $L_t = L_e + L_J$, the participation ratio $p = L_J/L_t$, the resonance frequency $\omega_r = 1/\sqrt{L_t C_e}$ and the quality factor $Q = \omega_r L_t / R_e$ we can rewrite this as

$$\ddot{q} + \frac{\omega_r}{Q} \dot{q} + \omega_r^2 q + \frac{p \dot{q}^2 \ddot{q}}{2I_0} = \frac{V_e}{L_t} \cos(\omega_m t) \quad (2.11)$$

Chapter 3

Realizing a Two-Qubit Processor

This chapter discusses the main experimental results of this thesis. We start by discussing the implementation of a superconducting two-qubit processor, discussing the characteristics of the Transmon qubits used in the processor, the readout scheme, single-qubit manipulation, two-qubit gates as well as the experimental procedures used for quantum state and quantum process tomography. The last section of this chapter will discuss the implementation of a quantum algorithm – so called Grover search algorithm – using our two-qubit processor and the demonstration of quantum speed-up achieved with our system.

3.1 Introduction & Motivation

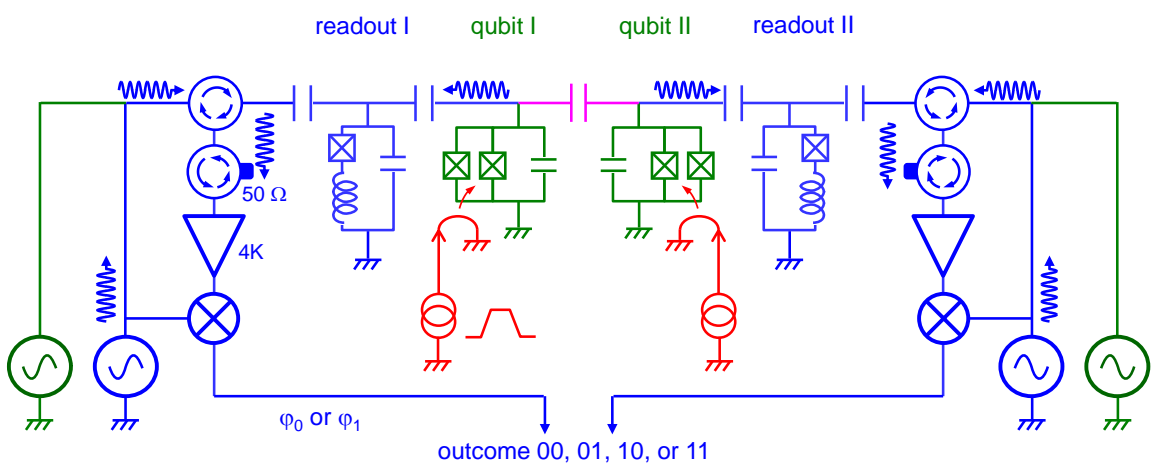


Figure 3.1: The circuit schematic of the two-qubit processor used in this work. Shown are the two Transmon qubits in green, the drive and readout circuit in blue, the fast flux lines in red and the coupling capacitance in magenta.

As discussed in the introduction, the most simple, usable quantum processor contains two qubits that are coupled by an universal two-qubit gate and which in addition

can be manipulated and read out individually. We realized such a two-qubit processor using two Transmon qubits, coupled through a fixed capacitance and readout out by individual single-shot readout of the JBA type. The circuit diagram of our processor is shown in fig. 3.1, showing the qubits, the drive and readout circuit and the coupling element between them. The following sections we'll discuss the parameters of individual parts of the processor.

3.2 Qubit Design

The parameters of the sample have been chosen in accordance to various design constraints of the qubit processor. For the qubits, the main design goals were high coherence time, good frequency tunability and fast drivability. As we will show later, the coherence time of the qubit is limited by relaxation to the ground state and coupling to external noise sources. The relaxation component of the Transmon qubit is ultimately limited by internal losses of the Josephson junction but usually is bound by coupling to the electromagnetic environment, as will be discussed later. The frequency tunability is important for the realization of fast two-qubit gates but can also limit the relaxation and coherence time of the qubit by coupling to external noise sources. The drivability speed on the other hand is limited by the anharmonicity of the qubit, which can however not be increased arbitrarily since it will make the qubit sensitive to charge noise when chosen too high. For the readout, the main design goals were readout speed and fidelity. The speed of the readout is limited by the quality factor of the readout resonator, which however also can induce qubit relaxation through the Purcell effect and may therefore not be chosen too small.

In the following paragraphs we'll therefore discuss the parameter design for our two-qubit processor and analyze the sample parameters that have been obtained.

3.3 Readout Design

3.4 Processor Fabrication

In this section we will discuss the fabrication of the two-qubit processor realized in this work.

Chapter 4

Measurement Setup

Fig. 4.1 show the measurement setup used for the two-qubit experiments. The different signal and measurement lines as well as the room-temperature and cryogenic microwave components used in our experiments will be described in the following paragraphs.

In this section we discuss the details of the measurement setup used to perform the two-qubit experiments presented in this thesis. All experiments have been performed in a custom-built dilution cryostat at $< 40 \text{ mK}$ using a cryogenic microwave signal generation and measurement chain. The individual components of this setup will be discussed in the following sections.

4.1 Sample Holder & PCB

The qubit chip is first glued to a high-frequency PCB **!6!**, then wirebonds are used to connect the groundplane and the center conductors of the on-chip transmission lines to their counterparts on the PCB. Finally, additional bond wires connect isolated ground planes on-chip. The realization of a good and uniform groundplane on the qubit chip and around is very important to suppress unwanted resonance modes that can be created when the connection between isolated ground planes is not good enough **!7!**. The mounted chip on the PCB is then placed in a Copper or Aluminium sample holder which fully encloses the PCB and serves to reduce unwanted couplings to the environment. The coplanar waveguides on the PCB are connected to Mini-SMP cables through a set of connectors that are soldered on the PCB.

To Do 6: add substrate material details

To Do 7: Add references e.g. to Schuster's thesis

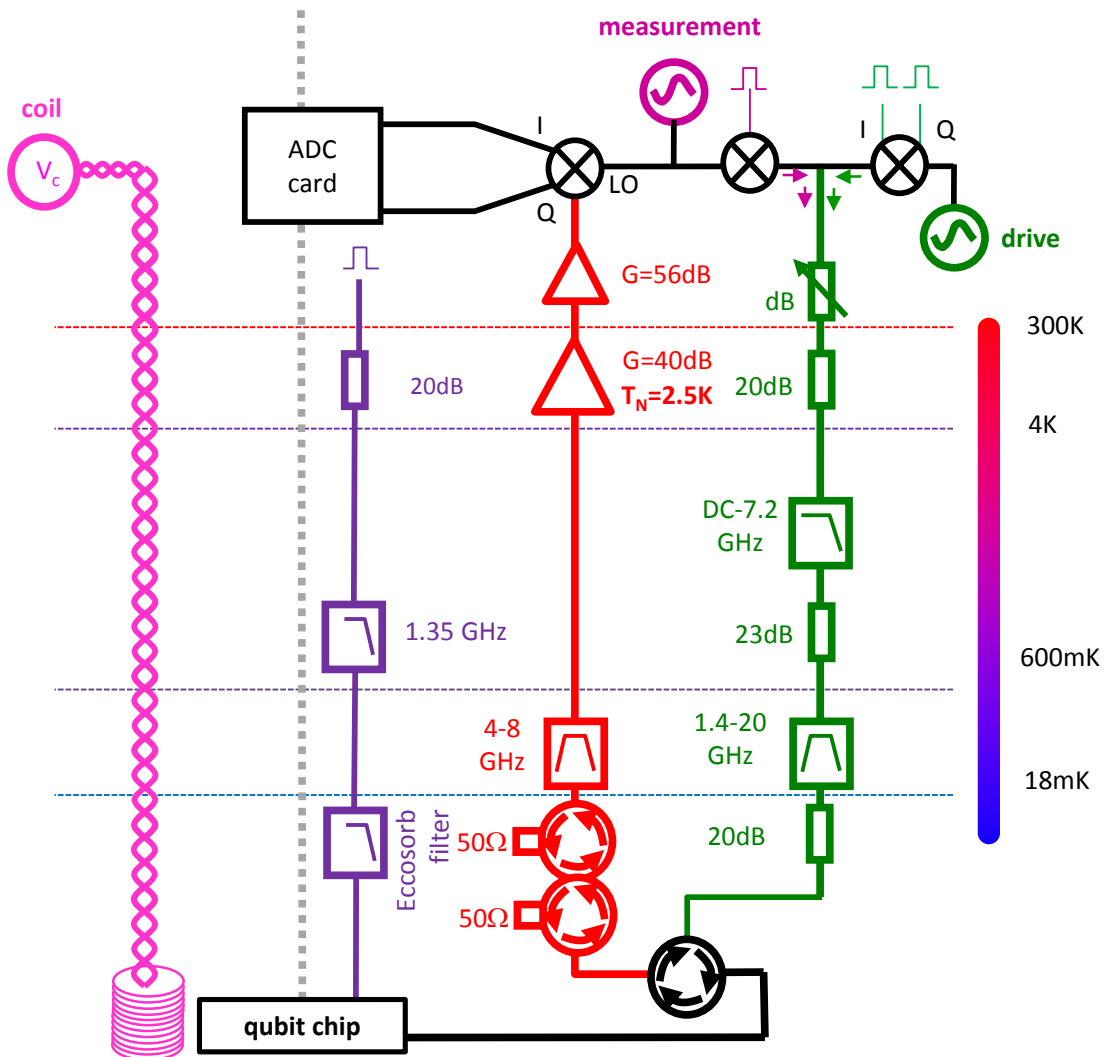


Figure 4.1: The measurement setup used for the two-qubit experiments. Exactly the same drive and readout scheme is used for both qubits with phase-locked microwave sources and arbitrary waveform generators.

4.2 Cryogenic Wiring

For the transmission of microwave signals to our sample we use various types of transmission lines suited for room-temperature and cryogenic application. The main goal of the input lines is to provide adequate signal transmission without introducing too much thermal conductance to the system. For the signal lines that carry the measurement signal from the sample we use superconducting cables [!8!](#) and low-resistance copper cables. In addition, we use superconducting bifilar cables for the DC bias of our magnetic coils. The qubit and fluxline input lines are attenuated and filtered at several stages of the cryostat to reduce signal noise.

To Do 8: add type

4.3 Signal Generation & Acquisition

Here we discuss the generation and acquisition of the different signals used to manipulate and read out our quantum processor. The experiments that have been performed require the generation, measurement and demodulation of microwave signals, the generation of fast flux control pulses and the application of DC currents to our magnetic coils.

4.3.1 Microwave Sideband Mixing

For qubit manipulation it is often advantageous to use single-sideband mixing for driving the qubit since it can provide higher ON/OFF ratios for microwave pulses and allow the driving of higher qubit-levels using a single, phase-coherent microwave source. To realize this, we use IQ mixers (Hittite [!9!](#)) that we drive with a continuous single-frequency microwave tone and two time-synchronized fast control signals generated by an arbitrary waveform generator (Tektronix AWG5014b). When feeding a signal $LO(t) = i_0 \cos(\omega_{rft}t)$ to the LO port of the mixer and two signals $I(t), Q(t)$ to the I and Q ports of the mixer one obtains a signal

$$RF(t) = I(t) \cos(\omega_{rft}t) + Q(t) \sin(\omega_{rft}t) \quad (4.1)$$

To Do 9: Add exact type number

at the LO port of the mixer. Since the IQ mixer that we use is a passive, reciprocal device one can as well feed two input signals to the LO and RF ports and obtain the demodulated signal quadratures at the I and Q ports, a technique that we'll make use of for our qubit readout scheme.

Commercially available IQ mixers often deviate from the ideal behavior as given by eq. (4.1). Typical imperfections include large insertion losses –i.e. loss of signal power between the different ports of the mixer–, RF signal leakage at zero IQ-input and frequency-dependent phase and amplitude errors of the mixed sideband signals. In order to achieve reliable single-qubit operations we need to correct the signal leakage and quadrature-specific amplitude and phase errors. The signal leakage causes a small part of the LO signal to leak through to the RF port even when the IQ inputs are zeroed. This leakage can be compensated by adding center-frequency ω_c dependent DC offset voltages to the IQ ports. The appropriate offset voltages can be determined by applying a continuous input signal at a frequency ω_c to the LO port of the mixer and minimizing the signal power at the RF port by varying the IQ offset voltages. To correct the sideband amplitude and phase errors we apply another correction procedure that we outline here. First, for the signals at the IQ inputs of the mixer we introduce the notation

$$A(t) = I(t) + iQ(t) = a(t) \exp(-i\phi(t)) \quad (4.2)$$

We consider an IQ signal at a single sideband frequency ω_{sb} and at fixed complex amplitude $a(t) = a = a_0 \exp(i\phi_0)$ such that $A(t) = a \exp(-i\omega_{sb}t)$. The effect of the gain and phase imperfections of the IQ mixers can then be modeled by assuming that the mixer adds another IQ signal $\epsilon(\omega_{sb}, \omega_c)A^*(t)$ at the mirrored sideband frequency $-\omega_{sb}$. We can correct this unwanted signal by adding a small correction $c(\omega_{sb}, \omega_c)A^*(t)$ to our IQ input signal. The correction coefficient $c(\omega_{sb}, \omega_c)$ usually depends both on the carrier frequency ω_c and the sideband frequency ω_{sb} . We determine the correction coefficients by generating a continuous waveform at a given center and sideband frequency, measuring the amplitude of the unwanted sideband signal with a fast spectrum analyzer and minimizing its amplitude by varying the correction coefficient $c(\omega_{sb}, \omega_c)$.

Both the offset and the sideband-amplitude and -phase corrections have been automatized using our data acquisition software, the resulting correction coefficients are summarized in fig. ??.

4.3.2 Fast Magnetic Flux Pulses

The fast flux lines are implemented by a pair of superconducting 50Ω transmission lines, which are attenuated by 20 dB and filtered at the 4K and 20 mK stages of the cryostat. The filtering at the 20 mK stage is realized through custom-made, highly absorptive Eccosorb filters. Fig. ?? shows an image of these filters and the attenuation characteristic obtained. The heavy filtering of the flux line greatly reduces noise seen by the qubit but also distorts all signals sent through the line. This distortion is unwanted especially at high frequencies and needs to be corrected. To do this we need to measure and compensate the frequency response of the flux line at experimental conditions. In order to do this, we feed back the flux signal sent to the sample through a transmission line which is exactly equivalent to the input line. This allows us to measure the returning signal at room temperature and – assuming symmetric distortion in the in-

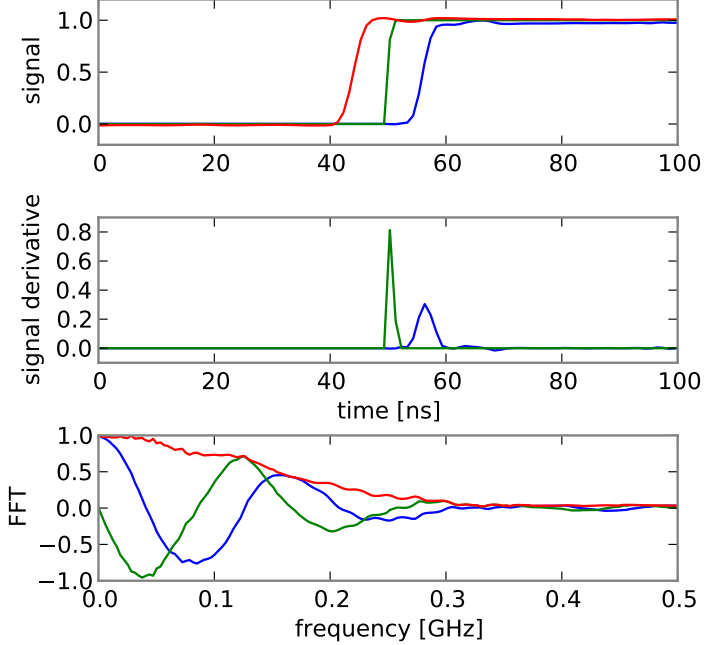


Figure 4.2: (response function filtered with a Gaussian filter with a cut-off at 0.4 GHz)

put and return line – to calculate the response function of the input line. Fig. 4.2 shows the different parts of the response function of the flux line as measured in our experiment. After eliminating the response of the analog-to-digital converter we can calculate the response function between the input port of the flux line and the sample by solving the equation

$$\dots \quad (4.3)$$

4.3.3 Pulse Synchronization

Chapter 5

Measurement Techniques

In this section we will discuss the techniques used to characterize and manipulate our two-qubit processor. All techniques employed are based on ...

5.1 Qubit Readout

5.2 Qubit Manipulation

5.3 Decoherence Time Measurement

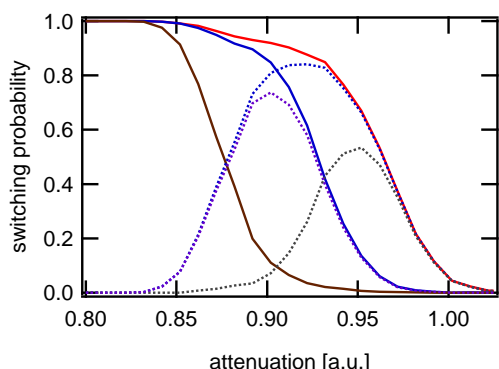


Figure 5.1: Example of a single-qubit s-curve measurement. Shown is the switching probability of the readout for a range of readout drive attenuations, for the different qubit states $|0\rangle$, $|1\rangle$ and $|2\rangle$. The difference in switching probability between individual curves defines the readout contrast between the corresponding qubit states at a given readout power attenuation.

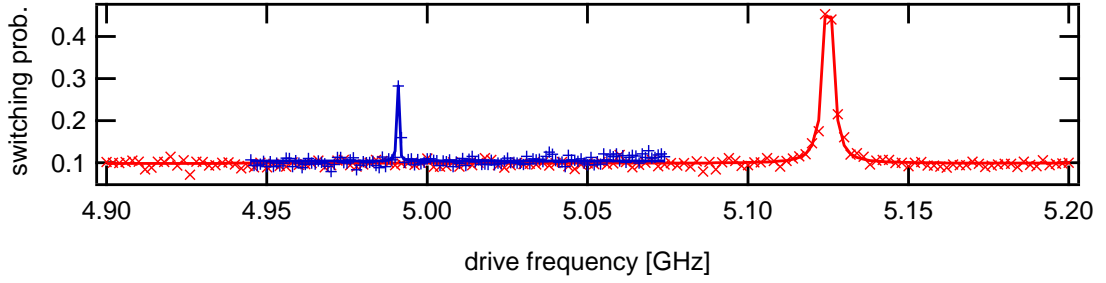


Figure 5.2: Example of a measured qubit spectroscopy. Shown is the switching probability of the qubit readout when driving the qubit with a very long drive pulse (typically $1 \mu\text{s}$) at a given drive frequency. The resonance to the right corresponds to the $|0\rangle \rightarrow |1\rangle$ (at frequency f_{01}) transition of the qubit, the resonance on the left to the 2-photon $|0\rangle \rightarrow |2\rangle$ (at frequency $f_{02}/2$) transition. We perform a Lorentzian fit of the two resonances to obtain the $|0\rangle \rightarrow |1\rangle$ and $|0\rangle \rightarrow |2\rangle/2$ resonance frequencies, from which we can calculate all other qubit transition frequencies.

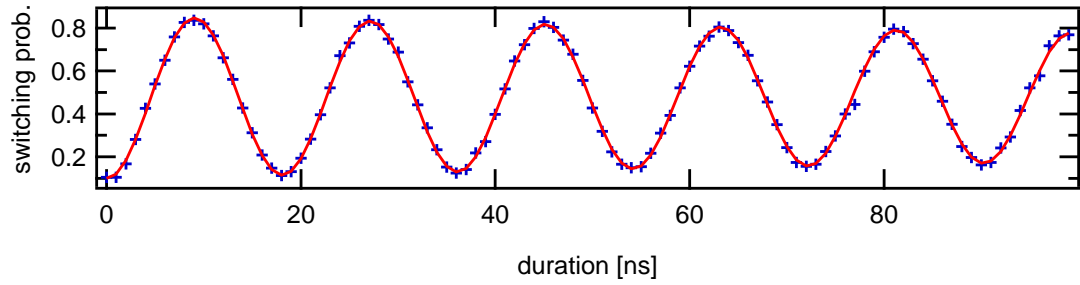


Figure 5.3: Example of a measured qubit Rabi experiment. Shown is the switching probability of the qubit readout when driving the qubit at f_{01} with a Gaussian drive pulse of varying duration. The measurement results are not corrected for readout errors.

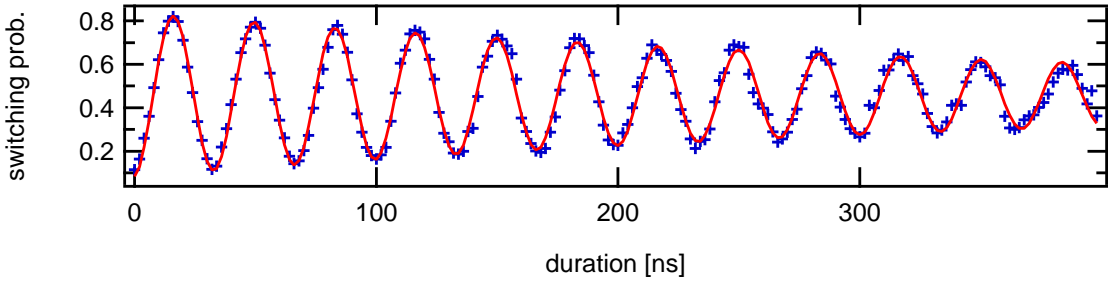


Figure 5.4: Example of a measured qubit Ramsey experiment. Shown is the switching probability of the qubit readout after performing a $X_{\pi/2}$ -wait- $X_{\pi/2}$ drive sequence at a frequency $f_{01} - \delta f$. Fitting the resulting curve with an attenuated sine-wave model allows us to determine the f_{01} frequency of the Qubit with high accuracy.

Chapter 6

Characterizing the Two-Qubit Processor

This section discusses the detailed characterization of individual circuit parts that will be used later to realize two-qubit gate and to run a quantum algorithm on the processor. The discussion will focus on the readout and microwave manipulation of the qubits as well as on the reconstruction of quantum states from measurement data, which will be used later for characterizing gate and processor operation.

6.1 Qubit & Readout Characterization

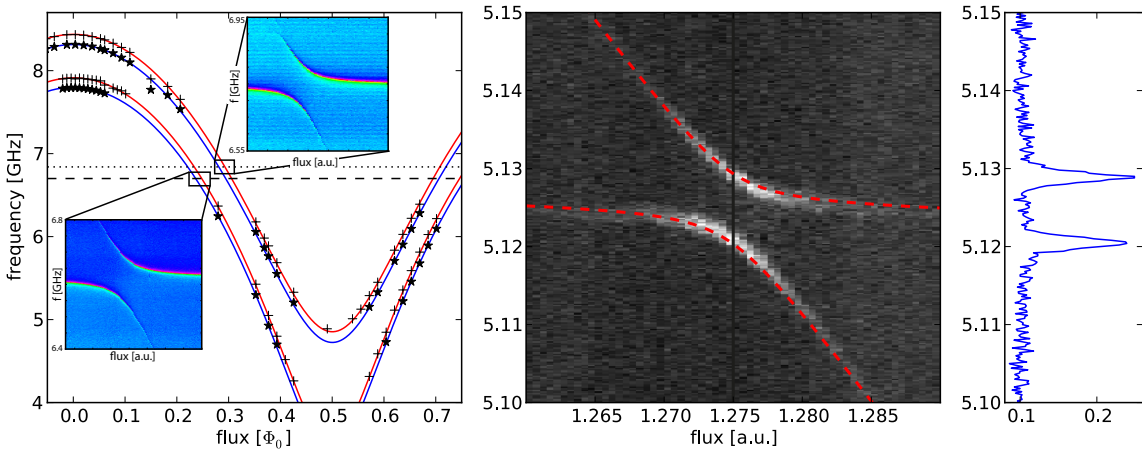


Figure 6.1: Spectroscopy of the realized two-qubit processor. a) $|0\rangle \rightarrow |1\rangle$ and $(|0\rangle \rightarrow |2\rangle)/2$ transition frequencies of the two qubits with fitted dependence and cavity frequencies. b) Avoided level crossing of the $|01\rangle$ and $|10\rangle$ levels of the qubits with fit, $g = 8.7$ MHz. c) Spectroscopy of qubit 1 at the point indicated in b).

The following section discusses the parameters of our two-qubit processor that have

been obtained by various measurements.

6.1.1 Qubit Parameters

To obtain all the relevant parameters of our two-qubit processor, we perform a set of measurements from which we obtain the qubit frequencies, anharmonicities, junction asymmetries, the inter-qubit coupling, the coupling to the microwave drive lines, the coupling of each qubit to its readout and the relaxation and dephasing times of the qubits. The drive and readout couplings as well as the relaxation and dephasing times are measured for a range of qubit frequencies, which will allow us later to pick an ideal working point for our two-qubit experiments. The qubit parameters obtained from spectroscopic measurements are as follows:

- *Qubits*: Spectroscopic measurement of the qubit transitions yielded parameter values of $E_J^I/h = 36.2$ GHz, $E_c^I/h = 0.98$ GHz and $E_J^{II}/h = 43.1$ GHz, $E_C^{II}/h = 0.87$ GHz for the Josephson and charging energies of the two qubits and values of $d^I = 0.2$, $d^{II} = 0.35$ for the qubit junction asymmetries.
- *Readout resonator*: The frequencies of the readout resonators have been measured as $\nu_R^I = 6.84$ GHz and $\nu_R^{II} = 6.70$ GHz with quality factors $Q^I \simeq Q^{II} = 730$, independent measurements of the Kerr nonlinearities yielded $K^I/\nu_R^I \simeq K^{II}/\nu_R^{II} = -2.3 \pm 0.5 \times 10^{-5}$!10! .
- *Qubit-Resonator coupling*: The coupling of the qubits to the readout resonators has been spectroscopically determined as $g_0^I \simeq g_0^{II} = 50$ MHz

To Do 10: add junction inferred parameters from the bare resonator frequencies

Readout Parameters

Qubit Readout, Driving, Relaxation and Dephasing Time

In order to obtain the relaxation time and the coupling of the qubit to the drive line, we perform an automated survey of qubit spectroscopies, qubit readout characterizations and T_1 measurements at different qubit frequencies. The results of such a parameter survey are summarized in fig 6.2, showing the relaxation time T_1 , the readout contrast c_{10} and the Rabi frequency f_{Rabi} for a fixed drive amplitude for the two qubits in a frequency range between 5.2 and 6.5 GHz. As can be seen, the relaxation time of the qubits tends to increase the farther detuned each qubit is from its readout resonator. Not surprisingly, the drive frequency of the qubit also decreases when the qubit-resonator detuning increases as expected from the Purcell effect, which filters incoming microwave signals that are far-detuned from the resonator frequency. The inverse is true for the readout contrast, which increases near-linearly when reducing the qubit-resonator detuning due

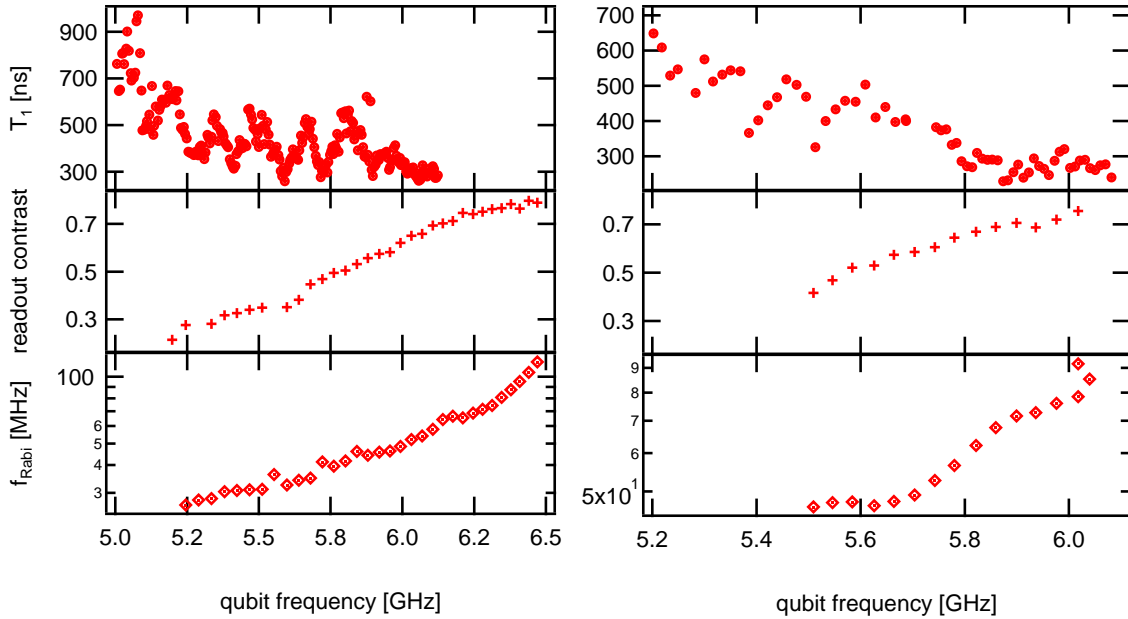


Figure 6.2: A qubit parameter survey showing the relaxation time T_1 , the readout contrast and the Rabi frequency at a fixed drive amplitude for the two qubits over a large range of qubit frequencies.

to the increase of the dispersive resonator frequency shift induced by the qubit that gets stronger the less the qubit is detuned from the readout resonator.

It is interesting to note the non-monotonous characteristic of the qubit relaxation time T_1 shown in fig. 6.2, which cannot be explained by Purcell-filtering through the readout resonator and hints at a different qubit relaxation process present in the system. A possible explanation would be the coupling of the qubit to a spurious low-Q resonance in the environment. Coupling to volumetric resonance modes of the sample holder or non-CPW resonance modes of the readout resonator can be possible explanations for the data. Also, the overall dependency of the relaxation time T_1 on the qubit-resonator detuning –ignoring the “fine-structure” present in the system– is not quadratic as would be expected from the Purcell theory but rather linear. Also, by comparing the qubit relaxation time to the Rabi drive frequency reveals that the increase in T_1 is clearly not proportional to the Purcell factor that determines the qubit relaxation rate through the readout resonator. However, the observed T_1 dependency can be partially explained by taking into account the qubit relaxation through the fast fluxline, which might be strongly-coupled to the qubit on our chip, hence inducing additional qubit relaxation beyond the Purcell and intrinsic qubit relaxation rates. This effect will therefore be studied in more detail in the following sections.

6.2 Single-Qubit Operations

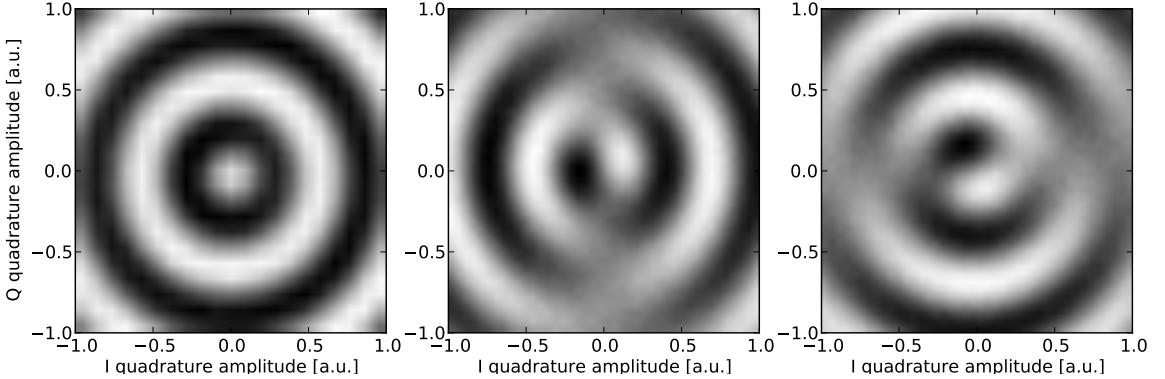


Figure 6.3: Demonstration of single-qubit IQ control. The figures show the state probability of a single qubit when preparing it in one of the states $|1\rangle$, $1/\sqrt{2}(|0\rangle+|1\rangle)$ or $1/\sqrt{2}(|0\rangle+i|1\rangle)$ and subjecting the qubit to a microwave drive pulse of the form $a(t) = V_I \cdot \cos \omega_{rf} t + V_Q \cdot \sin \omega_{rf} t$.

To perform arbitrary single-qubit operations – as needed e.g. for implementing a quantum algorithm or performing quantum state tomography – we need to implement a universal set of X , Y and Z qubit gates with our processor. Qubit rotations in the XY -plane are implemented through microwave drive pulses, where the phase of the drive pulse in reference to an arbitrary reference determines the rotation axis and the amplitude of the drive pulse the Rabi frequency of the gate. To characterize the drive pulses, we perform an experiment where we initialize a single-qubit in the states $|1\rangle$, $1/\sqrt{2}(|0\rangle+|1\rangle)$ and $1/\sqrt{2}(|0\rangle+i|1\rangle)$ and subject it afterwards to a single microwave pulse of the form $a(t) = V_I \cdot \cos \omega_{rf} t + V_Q \cdot \sin \omega_{rf} t$, which we tune by changing the input voltages V_I and V_Q to the IQ -mixer that generates the pulse from a continuous input microwave-tone at frequency ω_{rf} . We measure the qubit state at different values of V_I , V_Q , obtaining the graph shown in fig. 6.3. The qubit which was prepared in state $|1\rangle$ shows a perfectly cylinder-symmetric switching probability pattern when subjecting it to an IQ-pulse of a given phase, which is what one would expect for a qubit being prepared in either the $|0\rangle$ or $|1\rangle$ state. On the contrary, the switching probability distributions of the measured qubits prepared in the states $1/\sqrt{2}(|0\rangle+|1\rangle)$ and $1/\sqrt{2}(|0\rangle+i|1\rangle)$ are mirror-symmetric, where the switching probability does not vary at all along the drive axis which corresponds to the axis along which the qubit has been prepared. These measurements demonstrate therefore our ability to prepare and drive the qubit along arbitrary axes of the Bloch sphere. In the following sections we will analyze more in detail the drive errors inherent to our system and quantitatively analyze different error sources.

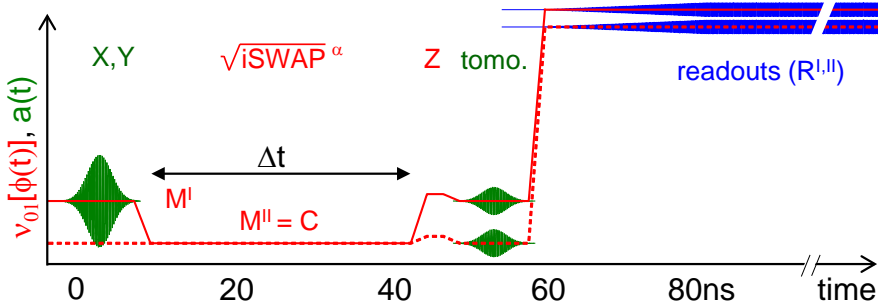


Figure 6.4

6.2.1 Estimation of drive errors

Since the Transmon is a weakly anharmonic multi-level system and thus no real qubit, driving the $|0\rangle \rightarrow |1\rangle$ transition with high power can induce transitions to higher Transmon levels. It is important to estimate and reduce these errors when performing fast qubit gates e.g. for state preparation or tomography. To model the driving of a Transmon, we use the simple drive model in the rotating-frame approximation and as used e.g. in Motzoi et al. (2009):

$$\hat{H} = \begin{pmatrix} 0 & \epsilon^*(t) & 0 \\ \epsilon(t) & \delta & \sqrt{2}\epsilon^*(t) \\ 0 & \sqrt{2}\epsilon(t) & 2\delta + \alpha \end{pmatrix} \quad (6.1)$$

Here, $\epsilon(t) = \epsilon_x(t) + i\epsilon_y(t)$ is the complex drive IQ amplitude in the rotating qubit frame, δ is the detuning of the microwave drive from the Transmon ω_{01} transition frequency and α is the Transmon anharmonicity. To estimate the leakage

6.3 Two Qubit Operations

6.3.1 Creation of Entanglement

6.3.2 Violation of the Bell Inequality

$$CHSH = QS + RS + RT - QT \quad (6.2)$$

with the operators Q, R, S, T being defined as

$$\begin{aligned} Q &= \sigma_z^1 & S &= \sigma_z^2 \cdot \cos \phi + \sigma_x^2 \cdot \sin \phi \\ R &= \sigma_x^1 & T &= -\sigma_z^2 \cdot \sin \phi + \sigma_x^2 \cdot \cos \phi \end{aligned} \quad (6.3)$$

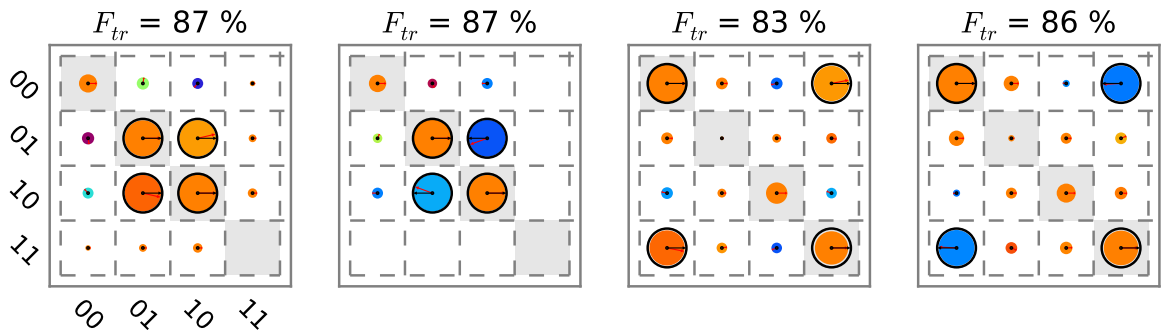


Figure 6.5: Experimentally created $|\psi_+\rangle$ ($F = 0.91$) and $|\psi_-\rangle$ ($F = 0.93$) states

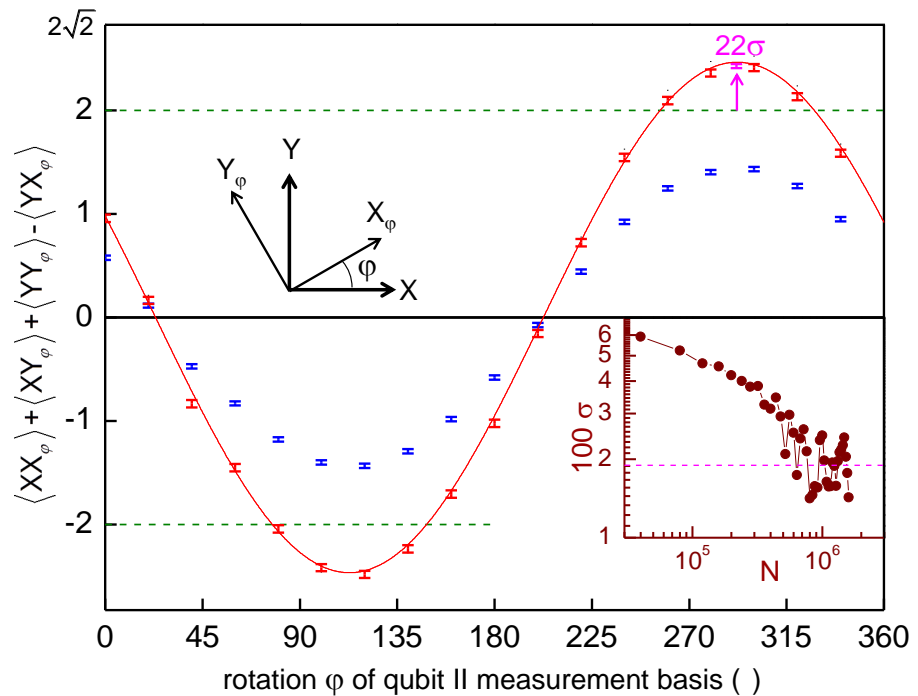


Figure 6.6

Here, the angle ϕ is a parameter that should be chosen in accordance to the phase of the Bell state on which it is applied.

6.3.3 Quantum State Tomography of Two-Qubit States

Quantum state tomography is the procedure of experimentally determining an unknown quantum state(Michael A. Nielsen and Isaac L. Chuang, 2000).

The density matrix of an n-qubit system can be written in general form as

$$\rho = \sum_{v_1, v_2, \dots, v_n} \frac{c_{v_1, v_2, \dots, v_n} \sigma_{v_1} \otimes \sigma_{v_2} \dots \otimes \sigma_{v_n}}{2^n} \quad (6.4)$$

$$c_{v_1, v_2, \dots, v_n} = \text{tr} (\sigma_{v_1} \otimes \sigma_{v_2} \dots \otimes \sigma_{v_n} \rho) \quad (6.5)$$

where $v_i \in \{X, Y, Z, I\}$ and n gives the number of qubits in the system and where the c_{v_1, v_2, \dots, v_n} are real-valued coefficients that fully describe the given density matrix. To reconstruct the density matrix of an experimental quantum system in a well-prepared state it is therefore sufficient to measure the expectation values of these $n^2 - 1$ coefficients on an ensemble of identically prepared systems. However, statistical and systematic measurement errors can yield a set of coefficients that corresponds to a *non-physical* density matrix which violates either the positivity or unity-trace requirement. In the following paragraph we will therefore discuss a technique with which one can estimate the density matrix of a system in a more correct way.

Maximum Likelihood Estimation of Quantum States

A method which is often used in quantum state tomography is the so-called *maximum-likelihood* technique. Rather than directly calculating the density matrix of the system from the obtained expectation values c_{v_1, v_2, \dots, v_n} , it calculates the joint probability of measuring a set $\{c_{X, X, \dots, X}, c_{Y, X, \dots, X}, \dots, c_{I, I, \dots, I}\}$ for a given estimate of the density matrix $\hat{\rho}$. By numerically or analytically maximizing this joint probability over the set of possible density matrices we obtain the density matrix which is most likely to have produced the set of measurement outcomes that we have observed.

The joint measurement operators $\Sigma_j = \sigma_{v_1} \otimes \sigma_{v_2} \dots \otimes \sigma_{v_n}$ have the eigenvalues ± 1 and can thus be written as

$$\sigma_{v_1} \otimes \sigma_{v_2} \dots \otimes \sigma_{v_n} = |+_j\rangle\langle +_j| - |-_j\rangle\langle -_j| \quad (6.6)$$

where $|+_j\rangle$ and $|-_j\rangle$ are the eigenstates corresponding to the eigenvalues ± 1 of Σ_j .

The expectation value $\langle \Sigma_j \rangle$ can be estimated by the quantity

$$\widehat{\langle \Sigma_j \rangle}_\rho = \frac{1}{l} \sum_{i=1}^l M_i(\Sigma_j, \rho) \quad (6.7)$$

where $M_i(M, \rho)$ denotes the outcome of the i -th measurement of the operator M on the state described by the density matrix ρ . This quantity is binomially distributed with the expectation value $E(\widehat{\langle \Sigma_j \rangle}_\rho) = \langle \Sigma_j \rangle_\rho$ and the variance $\sigma^2(\widehat{\langle \Sigma_j \rangle}_\rho) = 1/l \cdot (1 - \langle \Sigma_j \rangle_\rho^2)$. For large sample sizes l , the binomial distribution can be well approximated by a normal distribution with the same expectation value and variance. The joint probability of obtaining a set of measurement values $\{s_1, \dots, s_{n^2-1}\}$ for the set of operators $\{\widehat{\langle \Sigma_1 \rangle}_\rho, \dots, \widehat{\langle \Sigma_{n^2-1} \rangle}_\rho\}$ is then given as

$$P\left(\widehat{\langle \Sigma_1 \rangle}_\rho = s_1; \dots; \widehat{\langle \Sigma_{n^2-1} \rangle}_\rho = s_{n^2-1}\right) = \prod_{i=1}^{n^2-1} \exp\left(-\frac{l}{2} \frac{(s_i - \langle \Sigma_i \rangle_\rho)^2}{1 - \langle \Sigma_i \rangle_\rho^2}\right) \quad (6.8)$$

By maximizing this probability (or the logarithm of it) we obtain an estimate of the density matrix ρ of the quantum state. This technique also allows us to include further optimization parameters when calculating the joint probability. This is useful for modeling e.g. systematic errors of the measurement or preparation process, which can be described by modifying the operators contained in the probability sum. A common source of errors in our tomography measurements are errors in the microwave pulses used to drive the qubit. Since our measurement apparatus permits us only to measure the σ_z operator of each qubit we have to perform $\pi/2$ rotations about the Y or $-X$ axes of the Bloch sphere of each individual qubit in order to measure the values of the σ_x and σ_y operators, which we therefore replace with an effective measurement of each qubits σ_z operator preceded by a rotation R_{ν_i} given as

$$R_X = \exp(-i\sigma_y\pi/4) \quad (6.9)$$

$$R_Y = \exp(+i\sigma_x\pi/4) \quad (6.10)$$

Phase and amplitude errors can be modeled as

$$R_X = \exp(-i[+\sigma_y \cos \alpha + \sigma_x \sin \alpha] [\pi/4 + \gamma]) \quad (6.11)$$

$$R_Y = \exp(+i[-\sigma_y \sin \beta + \sigma_x \cos \beta] [\pi/4 + \delta]) \quad (6.12)$$

Here, α and β represent phase errors whereas γ and δ represent amplitude errors in the drive pulses.

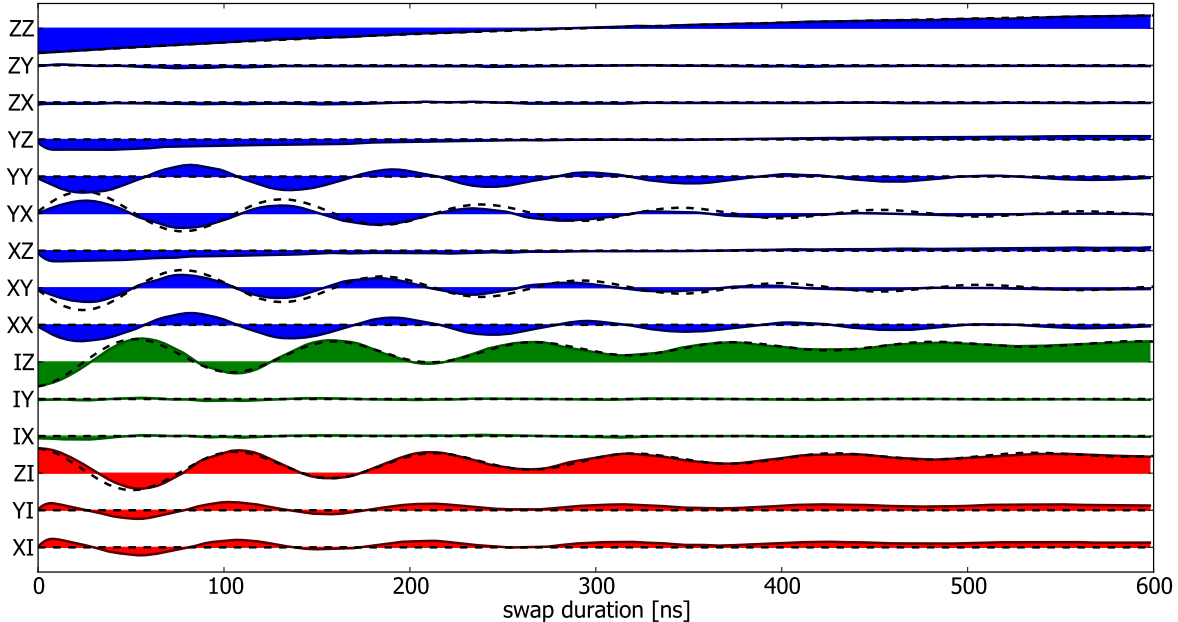


Figure 6.7: Measured Pauli operators $\sigma_i \otimes \sigma_j$ with $i, j \in \{X, Y, Z, I\}$ as a function of the interaction time. Shown are the 6 single-qubit operators as well as the 9 two-qubit correlation operators. The dashed line represents a master-equation simulation of the experiment.

6.4 Realizing a Two-Qubit Gate

6.4.1 Principle

6.4.2 Experimental Implementation

6.4.3 Quantum Process Tomography of the Gate

Introduction & Principle

Implementation

A quantum process can be described as a map $\mathcal{E} : \rho_{\mathcal{H}} \rightarrow \rho_{\mathcal{H}}$ that maps a density matrix ρ defined in a Hilbert space \mathcal{Q}_1 to another density matrix $\mathcal{E}(\rho)$ defined in a target Hilbert space \mathcal{Q}_2 and fulfilling three axiomatic properties Michael A. Nielsen and Isaac L. Chuang (2000); Haroche and Raimond (2006):

Axiom 6.0.1. $\text{tr} [\mathcal{E}(\rho)]$ is the probability that the process represented by \mathcal{E} occurs, when ρ is the initial state.

Axiom 6.0.2. \mathcal{E} is a *convex-linear map* on the set of density matrices, that is, for probabilities $\{p_i\}$,

$$\mathcal{E} \left(\sum_i p_i \rho_i \right) = \sum_i p_i \mathcal{E}(\rho_i) \quad (6.13)$$

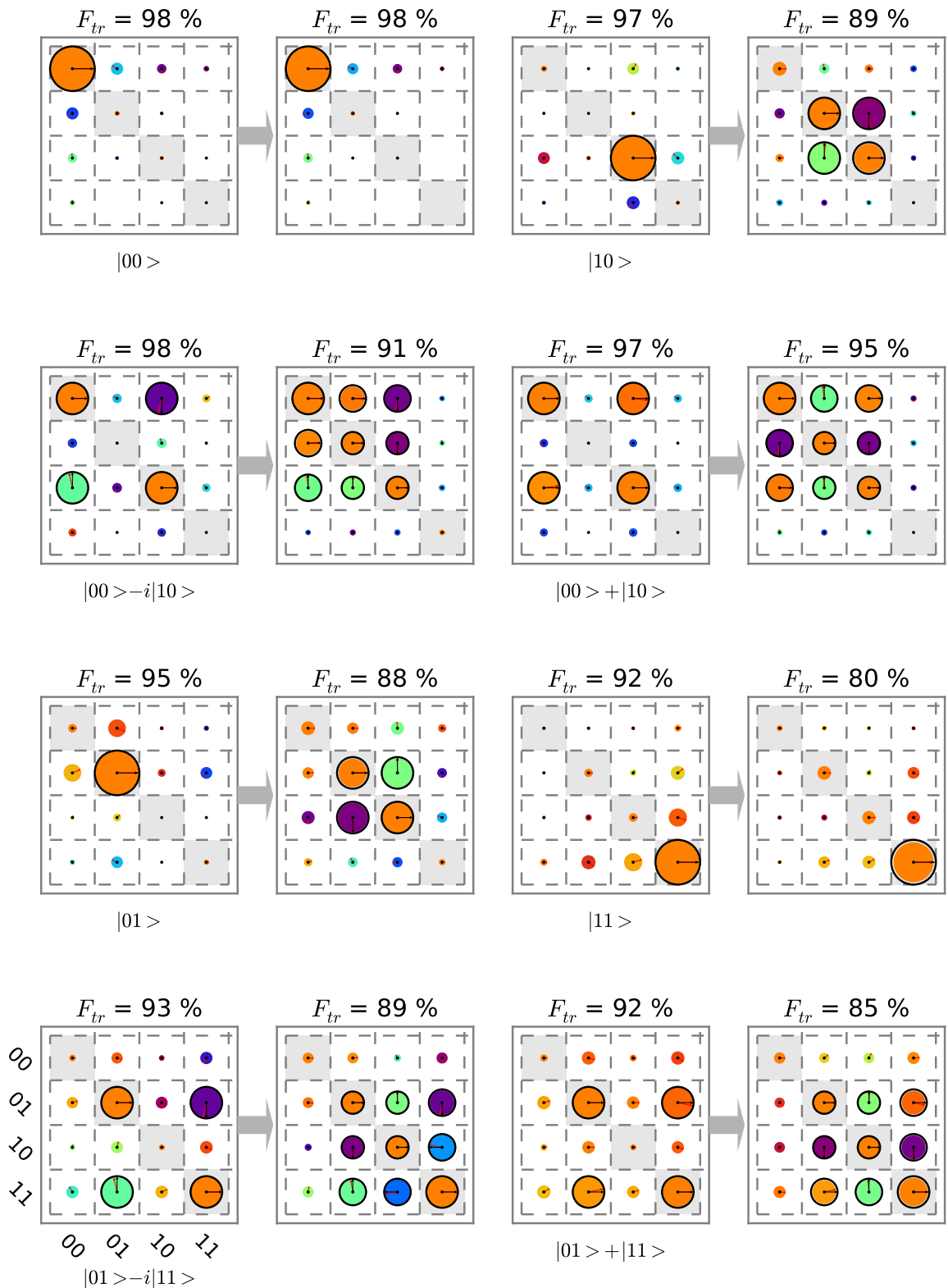


Figure 6.8: The input-output density matrix of the quantum process tomography of the $\sqrt{i\text{SWAP}}$ gate. Shown are the measured density matrices of 16 different input states and the corresponding output matrices with their state fidelities. The ideal matrices are overlaid in red.

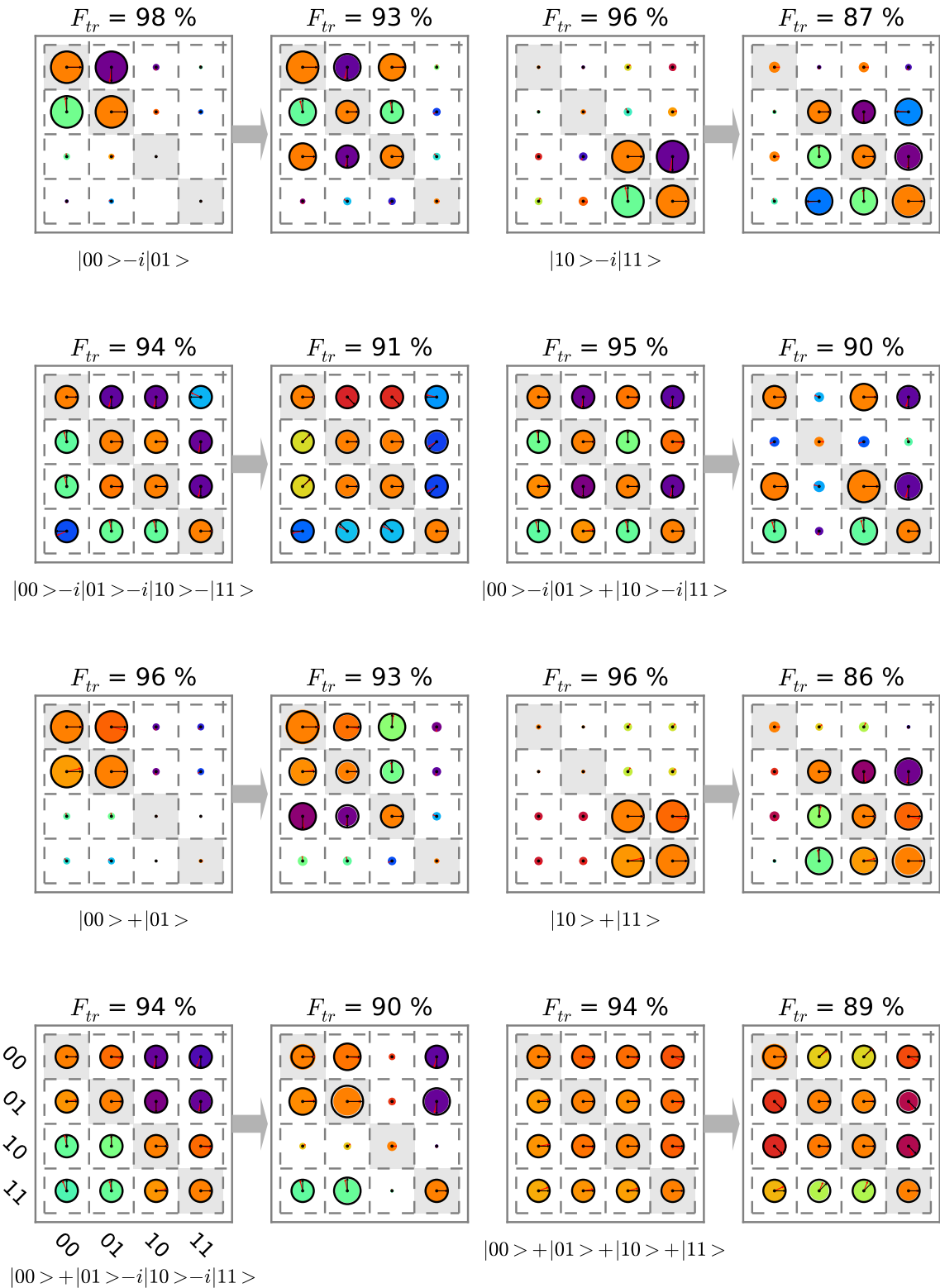


Figure 6.9: The input-output density matrix of the quantum process tomography of the $\sqrt{i}\text{SWAP}$ gate. Shown are the measured density matrices of 16 different input states and the corresponding output matrices with their state fidelities. The ideal matrices are overlaid in red.

Axiom 6.0.3. \mathcal{E} is a *completely-positive* map. That is, if \mathcal{E} maps density operators of system Q_1 to density operators of system Q_2 , then $\mathcal{E}(A)$ must be positive for any positive operator A . Furthermore, if we introduce an extra system R of arbitrary dimensionality, it must be true that $(\mathcal{I} \otimes \mathcal{E})(A)$ is positive for any positive operator A on the combined system RQ_1 , where \mathcal{I} denotes the identity map on system R .

As shown in Michael A. Nielsen and Isaac L. Chuang (2000), any quantum process fulfilling these criteria can be written in the form

$$\mathcal{E}(\rho) = \sum_i E_i \rho E_i^\dagger \quad (6.14)$$

for some set of operators $\{E_i\}$ which map the input Hilbert space to the output Hilbert space, and $\sum_i E_i^\dagger E_i \leq I$.

Now, if we express the operators E_i in a different operator basis \tilde{E}_j such that $E_i = \sum_j a_{ij} \tilde{E}_j$ and insert into eq. (6.14), we obtain

$$\mathcal{E}(\rho) = \sum_i \sum_j a_{ij} \tilde{E}_j \rho \sum_k a_{ik}^* \tilde{E}_k^\dagger \quad (6.15)$$

$$= \sum_{j,k} \tilde{E}_j \rho \tilde{E}_k^\dagger \sum_i a_{ij} a_{ik}^* \quad (6.16)$$

$$= \sum_{j,k} \tilde{E}_j \rho \tilde{E}_k^\dagger \chi_{jk} \quad (6.17)$$

where we defined $\chi_{jk} = \sum_i a_{ij} a_{ik}^*$. This is the so-called χ -matrix representation of the quantum process. Here, all the information on the process is contained in the χ matrix, which controls the action of the process-independent operators \tilde{E}_i on the initial density matrix ρ .

Now, the goal of *quantum process tomography* is to obtain the coefficients of the χ -matrix – or any other complete representation of the process – from a set of experimentally measured density matrices ρ and $\mathcal{E}(\rho)$.

To achieve this, several techniques have been developed. The technique used in this work is the so-called *standard quantum process tomography (SQPT)*. This technique proceeds as follows:

1. Choose a set of operators E_i that forms a full basis of $\mathcal{M} : Q_1 \rightarrow Q_2$. For n-qubit process tomography we usually choose $E_{i_1, i_2, \dots, i_n} = \sigma_{i_1} \otimes \sigma_{i_2} \dots \otimes \sigma_{i_n}$, where σ_i are the single-qubit Pauli operators and $i \in \{I, X, Y, Z\}$.
2. Choose a set of pure quantum states $|\phi_i\rangle$ such that $|\phi_i\rangle \langle \phi_i|$ span the whole space of input density matrices ρ . Usually, for a n-qubit system we choose $\phi =$

$\{|0\rangle, |1\rangle, (|0\rangle + |1\rangle)/\sqrt{2}, (|0\rangle + i|1\rangle)/\sqrt{2}\}^{\otimes n}$, where \otimes^n denotes the n-dimensional Kronecker product of all possible permutations.

3. For each of the $|\phi_i\rangle$, determine $\mathcal{E}(|\phi_i\rangle \langle \phi_i|)$ by quantum state tomography. Usually we also determine $|\phi_i\rangle \langle \phi_i|$ experimentally since the preparation of this state already entails small preparation errors that should be taken into account when performing quantum process tomography.

After having obtained the ρ_i and $\mathcal{E}(\rho_i)$ one obtains the χ -matrix by writing $\mathcal{E}(\rho_i) = \sum_j \lambda_{ij} \tilde{\rho}_j$, with some arbitrary basis $\tilde{\rho}_j$ and letting $\tilde{E}_m \tilde{\rho}_j \tilde{E}_n^\dagger = \sum_k \beta_{jk}^{mn} \tilde{\rho}_k$. We can then insert into eq. (6.17) and obtain

$$\sum_k \lambda_{ik} \tilde{\rho}_k = \sum_{m,n} \chi_{mn} \sum_k \beta_{ik}^{mn} \tilde{\rho}_k \quad (6.18)$$

This directly yields $\lambda_{ik} = \sum_{m,n} \beta_{ik}^{mn} \chi_{mn}$, which, by linear inversion, gives χ .

The Kraus Representation of the Quantum Process

Besides the χ -matrix representation, there is another useful way of expressing a quantum map, the so called *Kraus representation*, which is given as

$$\mathcal{E}(\rho) = \sum_i M_i \rho M_i^\dagger \quad (6.19)$$

It can be shown (Haroche and Raimond, 2006) that this sum contains at most N elements, where N is the dimension of the Hilbert space of the density matrix ρ . We can go from the χ representation to the Kraus representation by changing the basis \tilde{E}_i such that

$$\tilde{E}_i = \sum_l a_{il} \check{E}_l \quad (6.20)$$

which, for eq. (6.17), yields

$$\mathcal{E}(\rho) = \sum_{j,k} \sum_l a_{jl} \check{E}_l \rho \sum_m a_{km}^* \check{E}_m^\dagger \chi_{jk} \quad (6.21)$$

$$= \sum_{l,m} \check{E}_l \rho \check{E}_m^\dagger \sum_{j,k} a_{jl} a_{km}^* \chi_{jk} \quad (6.22)$$

The last sum on the right side of eq. (6.22) corresponds to a change of coordinates of the matrix χ . Now, we can pick the a such that χ is diagonal in the new basis \check{E} and obtain

$$\mathcal{E}(\rho) = \sum_l \lambda_l \check{E}_l \rho \check{E}_l^\dagger \quad (6.23)$$

$$= \sum_l M_l \rho M_l^\dagger \quad (6.24)$$

with λ_l being the l -th eigenvalue of the χ matrix with the eigen-operator \check{E}_l and $M_l = \sqrt{\lambda_l} \check{E}_l$.

6.4.4 Gate Fidelity

6.4.5 Gate Error Analysis

Tomographic errors are removed from the process map of our \sqrt{iSWAP} gate using the following method. The measured Pauli sets corresponding to the sixteen input states are first fitted by a model including errors both in the preparation of the state (index *prep*) and in the tomographic pulses (index *tomo*). The errors included are angular errors $\varepsilon_{I,II}^{\text{prep}}$ on the nominal π rotations around $X_{I,II}$, $\eta_{I,II}^{\text{prep,tomo}}$ and $\delta_{I,II}^{\text{prep,tomo}}$ on the nominal $\pi/2$ rotations around $X_{I,II}$ and $Y_{I,II}$, a possible departure $\xi_{I,II}$ from orthogonality of (\vec{X}_I, \vec{Y}_I) and $(\vec{X}_{II}, \vec{Y}_{II})$, and a possible rotation $\mu_{I,II}$ of the tomographic XY frame with respect to the preparation one. The rotation operators used for preparing the states and doing their tomography are thus given by

$$\begin{aligned} X_{I,II}^{\text{prep}}(\pi) &= e^{-i(\pi+\varepsilon_{I,II}^{\text{prep}})\sigma_x^{I,II}/2}, \\ X_{I,II}^{\text{prep}}(-\pi/2) &= e^{+i(\pi/2+\eta_{I,II}^{\text{prep}})\sigma_x^{I,II}/2}, \\ Y_{I,II}^{\text{prep}}(\pi/2) &= e^{-i(\pi/2+\delta_{I,II}^{\text{prep}})[\cos(\xi_{I,II})\sigma_y^{I,II}-\sin(\xi_{I,II})\sigma_x^{I,II}]/2}, \\ X_{I,II}^{\text{tomo}}(\pi/2) &= e^{-i(\pi/2+\eta_{I,II}^{\text{tomo}})[\sin(\mu_{I,II})\sigma_x^{I,II}+\cos(\mu_{I,II})\sigma_y^{I,II}]/2}, \\ Y_{I,II}^{\text{tomo}}(-\pi/2) &= e^{+i(\pi/2+\delta_{I,II}^{\text{tomo}})[\cos(\mu_{I,II}+\xi_{I,II})\sigma_y^{I,II}-\sin(\mu_{I,II}+\xi_{I,II})\sigma_x^{I,II}]/2}. \end{aligned}$$

The sixteen input states are then $\{\rho_{\text{in}}^e = U |0\rangle\langle 0| U^\dagger\}$ with $\{U\} = \{I_I, X_I^{\text{prep}}(\pi), Y_I^{\text{prep}}(\pi/2), X_I^{\text{prep}}(-\pi/2), X_{II}^{\text{prep}}(\pi), Y_{II}^{\text{prep}}(\pi/2), X_{II}^{\text{prep}}(-\pi/2)\}$, and each input state yields a Pauli set $\{\langle P_k^e \rangle = \text{Tr}(\rho_{\text{in}}^e P_k^e)\}$ with $\{P_k^e\} = \{I_I, X_I^e, Y_I^e, Z_I\} \otimes \{I_{II}, X_{II}^e, Y_{II}^e, Z_{II}\}$, $X^e = Y^{\text{tomo}}(-\pi/2)^\dagger \sigma_z Y^{\text{tomo}}(-\pi/2)$, and $Y^e = X^{\text{tomo}}(\pi/2)^\dagger \sigma_z X^{\text{tomo}}(\pi/2)$. Figure S5.1 shows the best fit of the modelled $\{\langle P_k^e \rangle\}$ set to the measured input Pauli sets, yielding $\varepsilon_I^{\text{prep}} = -1^\circ$, $\varepsilon_{II}^{\text{prep}} = -3^\circ$, $\eta_I^{\text{prep}} = 3^\circ$, $\eta_{II}^{\text{prep}} = 4^\circ$, $\delta_I^{\text{prep}} = -6^\circ$, $\delta_{II}^{\text{prep}} = -3^\circ$, $\eta_I^{\text{tomo}} = -6^\circ$, $\eta_{II}^{\text{tomo}} = -4^\circ$, $\lambda_I^{\text{tomo}} = 12^\circ$, $\lambda_{II}^{\text{tomo}} = 5^\circ$, $\xi_I = 1^\circ$, $\xi_{II} = -2^\circ$, and $\mu_I = \mu_{II} = -11^\circ$.

Knowing the tomographic errors and thus $\{\langle P_k^e \rangle\}$, we then invert the linear relation $\{\langle P_k^e \rangle = \text{Tr}(\rho P_k^e)\}$ to find the 16×16 matrix B that links the vector $\overrightarrow{\langle P_k^e \rangle}$ to the columnized density matrix $\overrightarrow{\rho}$, i.e. $\overrightarrow{\rho} = B \cdot \overrightarrow{\langle P_k^e \rangle}$. The matrix B is finally applied to the measured

sixteen input and sixteen output Pauli sets to find the sixteen $(\rho_{in}, \rho_{out})_k$ couples to be used for calculating the gate map.

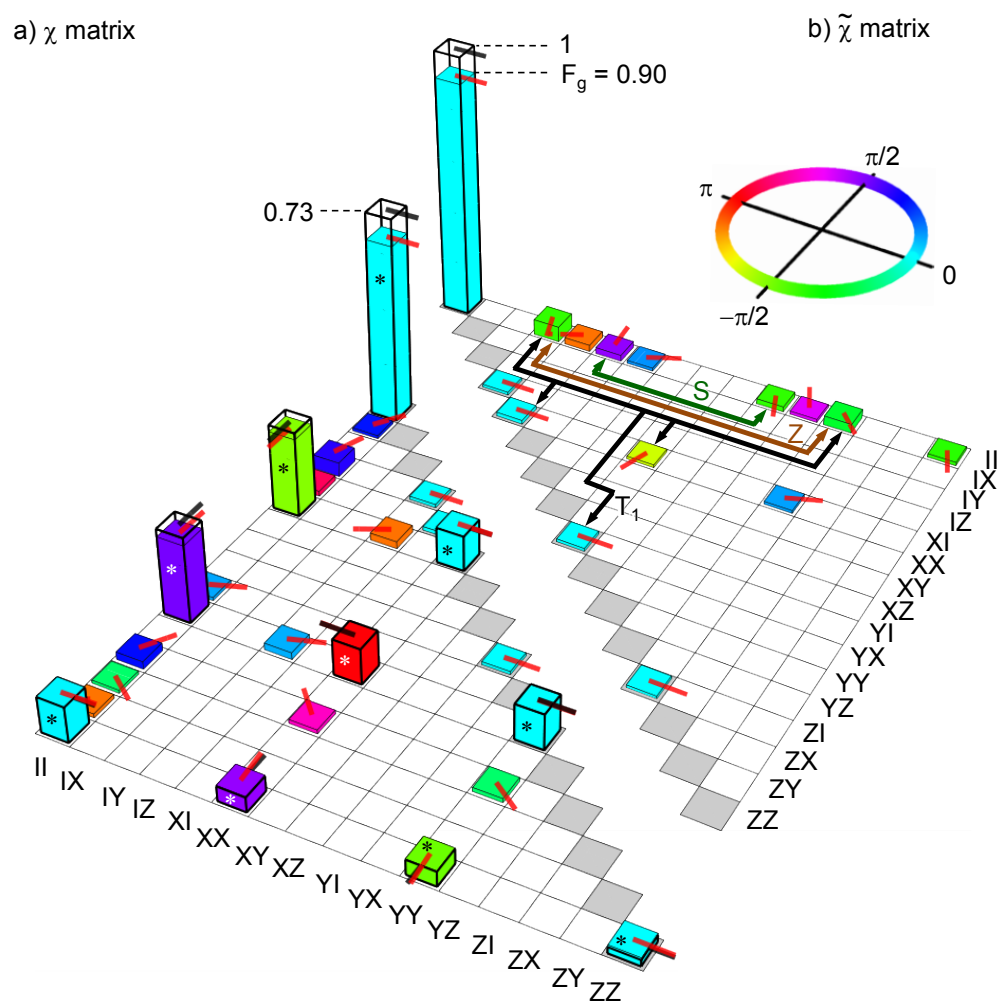


Figure 6.10

Chapter 7

Running the Grover Search Algorithm

This chapter will describe the experimental implementation of the so-called *Grover search algorithm* with our two-qubit quantum processor. The first section will provide a short introduction of the algorithm and motivate the interest in realizing it. The following sections will then discuss the details of the experimental realization of this algorithm. We will discuss the results that we obtained and compare the algorithm fidelity and runtime to that of an equivalent, classical algorithm. Finally, we will analyze all relevant errors made in our experiment.

7.1 Introduction & Motivation

Search algorithms are of great importance in many domains of mathematics and computer science. One such search problem that often arises and which will be discussed in the following sections can be formulated in simple terms as follows:

Theorem 7.1. Assume that we have a search space \mathcal{S} that consists of a finite number N of states $s \in \mathcal{S}$. The solution to our search problem corresponds to a finite subset of M states of the search space $\mathcal{T} \subset \mathcal{S}$. We can then define a search function $\mathcal{C}(s) : \mathcal{S} \rightarrow \{0, 1\}$ that discriminates between states that solve the search problem and states that don't, such that $\mathcal{C}(s) = 1$ for $s \in \mathcal{T}$ and $\mathcal{C}(s) = 0$ otherwise.

Using this definition of the search problem, the goal of a search algorithm is to find all states $t \in \mathcal{S}$ for which $\mathcal{C}(t) = 1$. In the following sections, for the sake of simplicity we will assume in the following sections that the solution set \mathcal{T} contains only one single state t . This special case can easily be generalized to cases where more than one solution exists to the search problem.

The first step in order to solve a search problem of the kind described above is to map the problem above to a form suitable for solution by a digital (quantum) computer. For this, we first number and encode the N input states $s_i \in \mathcal{S}$ in binary form such that

$s_i = \sum_{j=0}^l s_{ij} 2^j$, where l is the minimum required length of a binary register that can hold all N input states. With this definition, it is then also trivial to reformulate \mathcal{C} such that the function operates on a binary input register instead of the original input states.

Using these assumptions and definitions, it can then be shown that the most efficient classical search algorithm for solving the search problem above will use $\mathcal{O}(N)$ calls of the function \mathcal{C} to find the solution t of the search problem. Assuming that the time to evaluate the function \mathcal{C} is far superior to the time needed to perform any other operation during the search algorithm, the number of calls to \mathcal{C} also corresponds approximately to the runtime of the whole search algorithm.

Amazingly, in 1997, Grover (1997) found a quantum algorithm that could solve exactly the same search problem with only $\mathcal{O}(\sqrt{N})$ calls to the function \mathcal{C} . His algorithm achieves this by repeatedly calling a quantum-mechanical implementation of the function \mathcal{C} with a highly superposed qubit state and applying a special operator to the output state afterwards. The individual steps of the algorithm are straightforward and are given as follows:

1. Initialize a qubit register to the state $|\psi\rangle = |0\rangle$ (corresponding to a binary input state $|0000\dots 0_B\rangle$)
2. Apply the generalized Hadamard operation to the qubit register, producing a fully superposed quantum state

$$|\psi\rangle = \frac{1}{\sqrt{N}} \sum_{i=0}^{N-1} |i\rangle$$

3. Repeat the following sequence $\mathcal{O}(\sqrt{N})$ times:
 - a) Apply the *Oracle operator* $|i\rangle \rightarrow (-1)^{\mathcal{C}(i)} |i\rangle$ to the state $|\psi\rangle$
 - b) Apply the *diffusion operator* $|i\rangle \rightarrow -|i\rangle + \frac{2}{N} \sum_{j=0}^{N-1} |j\rangle$ to the state $|\psi\rangle$
4. Measure the state of the quantum register

Here, we have numerated the states of the qubit register from $|0\rangle$ to $|N-1\rangle$. The algorithm makes use of quantum parallelism to solve the search problem $\mathcal{O}(\sqrt{N})$ times faster than the most efficient classical algorithm. To understand better the action of the algorithm, the different steps of the Grover algorithm can be rephrased in the following, more intuitive way:

- First, it creates a fully superposed quantum state which contains all possible solutions to the search problem at once. The amplitudes and phases of each individual state are all equal in the beginning.

- Then, it applies the so-called Oracle operator to this superposed state. The effect of the Oracle is to flip the sign of the states t that corresponds to a solution of the search problem, i.e. for which $C(t) = 1$. As will be shown later, such an Oracle operator can be implemented in a straightforward way for any possible classical search function.
- In the next step, it applies a diffusion operator to the quantum state which transfers a fraction of the amplitude of all states with positive amplitude to the states with negative amplitude, increasing the amplitude of the latter in expense of the amplitude of the former. In this process, all states whose amplitude signs have been flipped get reset to positive values.
- Repeating these two operations increases the amplitude of the states which correspond to a solution of the search problem in a monotonous way until the amplitudes of all the other states are zero. When all the amplitude has been transferred to those states, the process reverses and the amplitude is transferred back to the other states. Hence it is crucial to stop the repeated application of the Oracle and diffusion operators after the right number of iterations.

As can be seen, the Grover algorithm uses quantum superposition as a resource to “crawl” a given search space faster than any possible classical algorithm, therefore speeding up the finding of a solution to the search problem. However, the crux of the algorithm is the way in which it extracts the knowledge of the search space it acquires when calling the search function with a superposed quantum state. This is very important since when applying the search function to a superposed quantum state the resulting output state will indeed contain the values of the search function for all possible values, but it is usually impossible to extract the full information from this state with one single measurement since any measurement performed on the qubit state will project it to an eigenstate of the measurement operator, thus destroying most of the information contained in the state. It would be possible to obtain the full information on the resulting quantum state by performing quantum state tomography, however for a N qubit register this would involve 2^N preparation and measurement cycles, thereby destroying any potential quantum-speed. It is therefore necessary to find a method by which one can extract the knowledge on the search function encoded in the quantum state in less than $\mathcal{O}(N)$ operations. This is exactly what the diffusion operator D achieves by converting the phase information contained in a superposition state to which the Oracle operator has been applied to a gain in amplitude of all states with negative amplitudes.

7.1.1 Deriving the Grover Algorithm from Schrödinger’s Equation

An interesting derivation of this algorithm starting from Schrödinger’s equation has

been given in a seminal paper by Grover (2001) and shall be briefly rediscussed here. The derivation begins by considering a quantum system governed by Schrödinger's equation, which can be written as (omitting all physical constants for the sake of clarity)

$$-i\frac{\delta}{\delta t}\psi(x, t) = \frac{\delta^2}{\delta x^2}\psi(x, t) - V(x)\psi(x, t) \quad (7.1)$$

Here $\psi(x, t)$ describes the wave-function and V is a time-independent potential. Let us assume that the potential $V(x)$ is shaped as in fig. 7.1, i.e. possessing a local minimum of energy. When one initializes the system to a state $\psi_0(x, t_0)$ and lets it evolve for a given time, the resulting state $\psi(x, t)$ will have a tendency to have a high probability density in the local minimum of the potential, thus “falling” into the potential minimum much like a classical system would.

It is thus interesting to ask if one could encode the solution to some hard problem as a point of minimum energy x_0 of a potential $V(x)$ and design an algorithm that would take an initial state $\psi_0(x, t_0)$ and let it evolve into a state that has a high probability around x_0 . Most problems in classical computer science involve functions operating on binary numbers of fixed length, so to encode these numbers we can discretize our wavefunction $\psi(x, t)$ using a regular grid of points x_i with a spacing dx , as shown in fig. 7.1b. When we discretize the time evolution of eq. 7.1 in steps dt as well and define $\epsilon = dt/dx^2$, we obtain a new equation of the form

$$-\frac{\psi_i^{t+dt} - \psi_i^t}{dt} = \frac{\psi_{i+1}^t + \psi_{i-1}^t - 2\psi_i^t}{dx^2} - V(x_i)\psi_i^t \quad (7.2)$$

where we have written $\psi(x_i, t) = \psi_i^t$. This equation can be written in matrix form as

$$\vec{\psi}^{t+dt} = S^t \cdot \vec{\psi}^t \quad (7.3)$$

with S being a state transition matrix of the form

$$S = \begin{pmatrix} 1 - 2i\epsilon - iV(x_1)dt & i\epsilon & 0 & \dots & i\epsilon \\ i\epsilon & 1 - 2i\epsilon - iV(x_2)dt & i\epsilon & \dots & 0 \\ 0 & i\epsilon & \ddots & & \vdots \\ \vdots & & & \ddots & \vdots \\ i\epsilon & 0 & \dots & i\epsilon & 1 - 2i\epsilon - iV(x_n)dt \end{pmatrix} \quad (7.4)$$

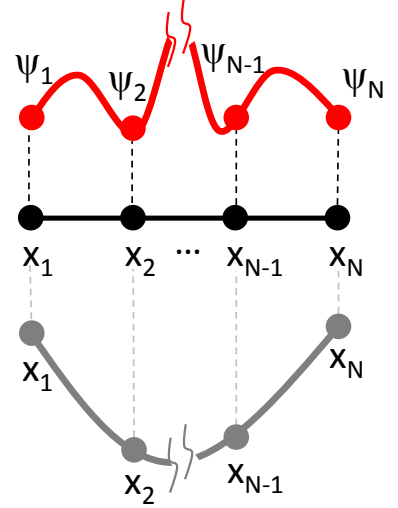


Figure 7.1: A wavefunction $\psi(x)$ and potential $V(x)$ defined on a grid of points x_1, \dots, x_N .

where we have used cyclic boundary conditions and defined $\epsilon = dt/dx^2$. To calculate the wavefunction at a finite evolution time we make use the Lie-Trotter formula

$$\exp(A + B) = \lim_{N \rightarrow \infty} (\exp(A/N) \exp(B/N))^N \quad (7.5)$$

to write $\exp(S) \approx D \cdot R$ with

$$D = \begin{pmatrix} 1 - 2i\epsilon & i\epsilon & 0 & 0 & \dots & i\epsilon \\ i\epsilon & 1 - 2i\epsilon & i\epsilon & 0 & \dots & 0 \\ \dots & \ddots & & & & \vdots \\ i\epsilon & 0 & 0 & \dots & i\epsilon & 1 - 2i\epsilon \end{pmatrix} \quad (7.6)$$

and

$$R = \begin{pmatrix} e^{-iV(x_1)dt} & 0 & \dots & 0 \\ 0 & e^{-iV(x_2)dt} & \dots & 0 \\ 0 & \dots & 0 & e^{-iV(x_N)dt} \end{pmatrix} \quad (7.7)$$

This approximation is correct to $\mathcal{O}(\epsilon)$ up to an unrelevant renormalization factor. The technique of splitting up the full evolution operator into a product of two or more non-commuting evolution operators that are applied successively is widely used in digital quantum simulation (Lloyd, 1996; Lanyon et al., 2011). We can now repeatedly apply the matrix product $D \cdot R$ to the wavefunction to obtain its state after a given finite time Δt by writing

$$\vec{\psi}^{t+\Delta t} = \left(\prod_{i=1}^{\Delta t/dt} D \cdot R \right) \cdot \vec{\psi}^t \quad (7.8)$$

As can be seen, the evolution of the wavefunction is governed by two processes: The interaction of the wavefunction with the potential V and a diffusion process which mixes different spatial parts of the wavefunction. The operator D resembles a Markov diffusion process since each row and column of the matrix sums up to unity, whereas R changes the phase of each element of the wavefunction in accordance with the local potential seen by it. If we apply R to a fully superposed initial state of the form $\psi_i = 1$ (we omit the normalization factor for clarity) and assume that $V_i = 0$ for $i \neq j$ and $V_j dt = \pi/2$, the element ψ_j will get turned according to $\psi_j \rightarrow i\psi_j$, whereas all other elements ψ_i will remain unchanged. Applying the operator D to the resulting state will transform ψ_j according to $\psi_j \rightarrow \psi_j(i + 2\epsilon(1 + i))$ with a corresponding amplitude $\sqrt{1 + 4\epsilon + \mathcal{O}(\epsilon^2)}$ and the adjacent states $\psi_{j\pm 1}$ according to $\psi_{j\pm 1} \rightarrow \psi_{j\pm 1}(1 - \epsilon(1 + i))$ with an amplitude $\sqrt{1 - 2\epsilon + \mathcal{O}(\epsilon^2)}$. Hence there is a transfer of amplitude between the state whose phase

has been turned and its neighboring states. If we reset the phases of all the ψ_i to zero afterwards, we can iterate the application of $D \cdot R$ until all of the amplitude has been transferred to the element ψ_j . This, in essence, is exactly what the Grover algorithm does with the only difference the matrix D gets replaced with an unitary matrix

$$D = \begin{pmatrix} -1 + 2/N & 2/N & 2/N & \dots & 2/N \\ 2/N & -1 + 2/N & 2/N & \dots & 2/N \\ \vdots & & \ddots & & \vdots \\ 2/N & 2/N & 2/N & \dots & -1 + 2/N \end{pmatrix} \quad (7.9)$$

and R with an unitary matrix

$$R = I^{N \otimes N} - 2 \sum_i C(i) |i\rangle \langle i| \quad (7.10)$$

that implements the quantum Oracle operator for the search function C . These matrices are chosen such that the transfer of amplitude between the marked state and the others is maximized in each step of the algorithm. By repeating the $D \cdot R$ sequence $\mathcal{O}(\sqrt{N})$ times with these modified matrices, all the amplitude can be transferred to the basis state $|j\rangle$ for which $C(j) = 1$, hence solving the search problem.

7.1.2 Ancilla-based Implementation of the Algorithm

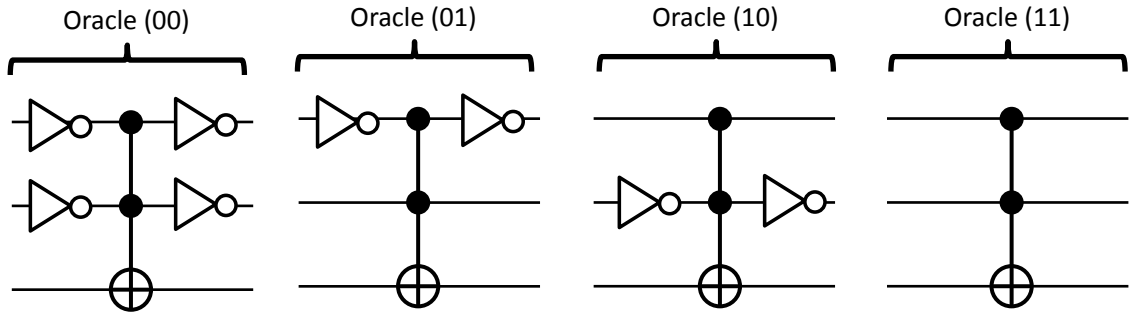


Figure 7.2: Implementations of the four possible Oracle functions used in the Grover search algorithm, using only reversible gate operations.

The implementation of the Grover search algorithm outlined above encodes the value of the search function C in the phase of the input state supplied to this function. This makes it hard to compare the algorithm to a classical search algorithm which operates on a binary input states and, in general, cannot encode the result of the search function directly in the input state. It is therefore useful to formulate a version of the Grover algorithm where the Oracle function does not directly encode the marked state in the input qubit register but uses an ancilla qubit to store the result of calling C . Such a representation of the algorithm is very useful since it can be directly compared to a

classical algorithm implemented with reversible logic gates, thus making it possible to benchmark our algorithm against a classical counterpart. Exemplary implementations of ancilla-based search functions \mathcal{C} implemented using quantum gates are shown in fig. 7.2 for the two-qubit case. There, a two-qubit Toffoli gate in combination with several single-qubit NOT gates (which can be easily implemented as single-qubit X_π rotations) is used to flip the state of an ancilla-qubit conditionally on the input state of the gate. Furthermore, any arbitrary classical search function \mathcal{C} that can be implemented with a set of universal reversible logic gates (e.g. the Toffoli gate and the NOT gate) can be directly mapped to a corresponding quantum operator that works on quantum-mechanical input states and implements the classical search function.

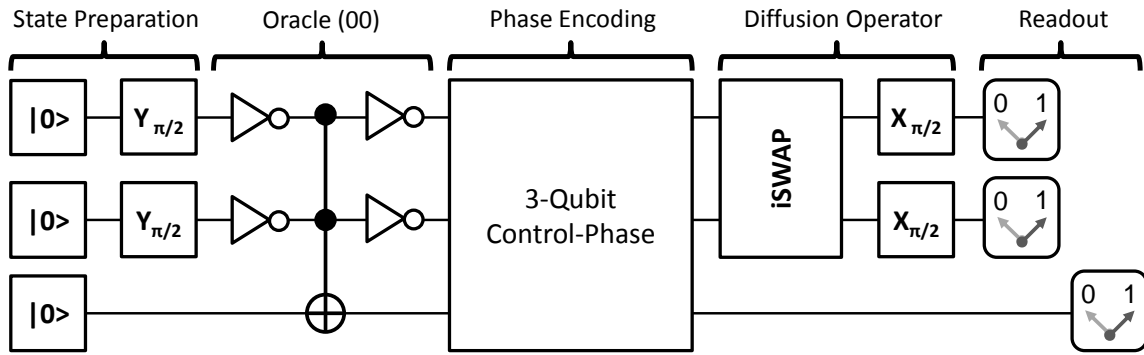


Figure 7.3: A full version of an implementation of the two-qubit Grover search algorithm. This algorithm works on a two-qubit input state and flips the state of a control qubit for one of the four possible input states in accordance to an unknown Oracle function. It then applies a 3-qubit control-phase operation of that maps $|xx1\rangle \rightarrow -|xx1\rangle$, $|xx0\rangle \rightarrow |xx0\rangle$ to encode the state of the control qubit directly in the two input qubits and then uses a diffusion operator to determine the state which has been marked by the Oracle function.

Fig. 7.3 shows a full ancilla-based implementation of the two-qubit Grover algorithm using the quantum Oracle function described above. This algorithm proceeds almost identically to version of the Grover algorithm discussed in the last section, with the only difference that after calling the Quantum oracle function it uses a three-qubit control-not (CNOT) gate C of the form

$$C = I^{n \otimes n} - 2 \sum_{ij} |ij1\rangle \langle ij1| \quad (7.11)$$

to phase-encode the state of the ancilla qubit into the state of the input qubit register. During the further operation of the algorithm, the ancilla qubit must not be read out since it will destroy the prepared state of the input qubit register otherwise. However, reading out the value of the ancilla qubit after the end of the algorithm allows one to check for the existence of a solution of the search problem, in which case the ancilla qubit will return a value of $|1\rangle$ upon readout.

7.2 Comparision to a Classical Algorithm

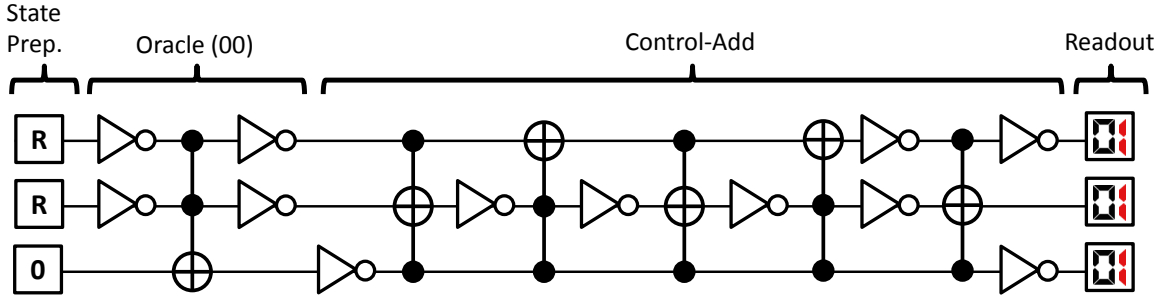


Figure 7.4: Classical reversible implementation of a search algorithm on a two-bit input register. The Oracle function can be implemented by two single-bit NOT operations and a Toffoli gate. R designates the generation of a random binary value at the beginning of the algorithm. If the Oracle does not yield the correct answer, the test state gets incremented. The average success probability of the algorithm is 50 %.

In order to quantify the quantum speed-up achieved for a certain quantum algorithm, it is necessary to formulate the problem solved by the quantum algorithm such that it can be compared to an equivalent problem that can be solved by a classical algorithm. The classical search problem solved by the Grover search algorithm has already been discussed in the first section of this chapter and with the ancilla-based version of the Grover algorithm that we introduced in the last section it is possible to directly compare the performance of a classical search algorithm with that of the Grover search algorithm. As has been discussed above, any possible Oracle function can be implemented both in quantum computing as well as classical computing using reversible logic gates such as the Toffoli gate and the single-(qu)bit NOT gate. Using this fact, we can devise a simple probabilistic algorithm that solves our search algorithm. This algorithm is shown in fig. 7.4 and achieves a success probability of 50 % by evaluating the function \mathcal{C} for a randomly generated two-qubit input value r . If $\mathcal{C}(r) = 1$, the algorithm directly returns r , otherwise it binary adds 1 to the state r and returns this incremented input state. By this technique, it achieves an average success probability of 50 % over all four possible Oracle functions. This 50 % success rate therefore provides a benchmark against which we will measure the speed-up of our implementation of the Grover algorithm.

7.3 Experimental Implementation

In this work we implement a compiled version of the two-qubit Grover algorithm. The gate sequence of the algorithm is shown in fig. 7.5 and consists in two i SWAP gates and six single-qubit gates applied to an initial state $|00\rangle$. The first i SWAP gate together with the two single-qubit $Z_{\pm\pi}$ rotations implements the Oracle function $f(x)$ as given in eq.

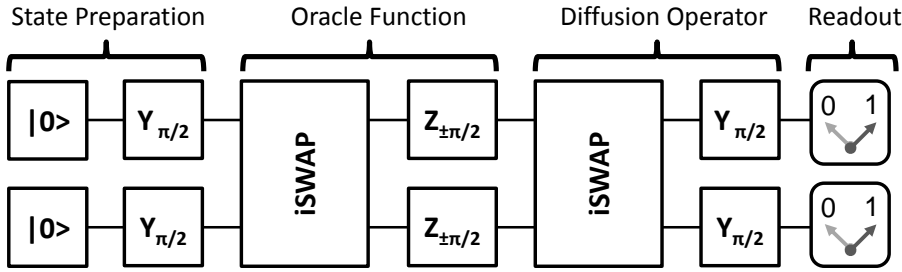


Figure 7.5: Schematic of our implementation of the Grover search algorithm. The algorithm consists in generating a fully superposed input state, applying the Oracle function to it and analyzing the resulting state by applying the Diffusion transform to it and reading out the value of the qubit register afterwards.

(7.10), where the signs of the rotation operations determines the state which is marked and can be either $|00\rangle$ (corresponding to a $Z_{-\pi/2}^1 \cdot Z_{-\pi/2}^2$ rotation), $|01\rangle$ ($Z_{-\pi/2}^1 \cdot Z_{\pi/2}^2$), $|10\rangle$ ($Z_{\pi/2}^1 \cdot Z_{-\pi/2}^2$) or $|11\rangle$ ($Z_{\pi/2}^1 \cdot Z_{\pi/2}^2$). The second *iSWAP* operation together with the following $X_{\pi/2}^1 \cdot X_{\pi/2}^2$ operation implements the diffusion operator as given by eq (7.9). The final step of the algorithm consists in reading out the two-qubit register.

7.3.1 Pulse Sequence

To implement the gate sequence described above we need to realize a sequence of microwave and flux pulses which realize the individual quantum gates of the sequence. To eliminate possible gate errors, we perform a series of calibration measurements before to tune-up the individual single- and two-qubit gates needed for the algorithm. In addition, we run individual parts of the algorithm successively and perform quantum state tomography to characterize the state of the quantum register after each step of the algorithm and correct the gate operations applied to the qubit in order to maximize the fidelity of the measured states in respect to the ideal ones. Fig. 7.6 shows an experimental pulse sequence for the Grover algorithm with an Oracle operator marking the state $|00\rangle$. Shown are the frequencies of the two qubits during the runtime of the algorithm and the microwave drive and readout pulses applied to them.

7.4 Results

Here we'll discuss the results obtained when running the Grover search algorithm with our two-qubit processor. In the first section we'll analyze the quantum state of the qubit register during the algorithm by performing quantum state tomography. In the second section we will present and discuss the single-run results obtained in our experiment.

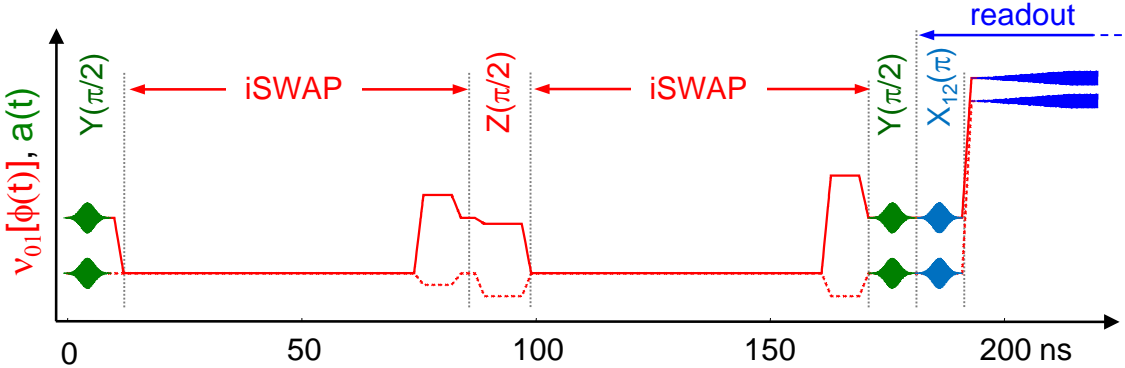


Figure 7.6: The pulse sequence used in realizing Grover’s quantum search algorithm. First, a $Y_{\pi/2}$ pulse is applied to each qubit to produce the fully superposed state $1/2(|00\rangle + |01\rangle + |10\rangle + |11\rangle)$. Then, an $i\text{SWAP}$ gate is applied, followed by a $Z_{\pm\pi/2}$ gate on each qubit, which corresponds to the application of the oracle function. The resulting state is then analyzed using another $i\text{SWAP}$ gate and two $Y_{\pi/2}$ gates to extract the state which has been marked by the oracle function. Optionally, a Y_{π}^{12} pulse is used on each qubit to increase the readout fidelity.

7.4.1 State Tomography of the Algorithm

Fig. 7.7 shows the results when running the Grover search algorithm for the four possible Oracle functions. Shown are quantum state tomographies after each step of the algorithm and the single-run results obtained when measuring the qubit register after the final step of the algorithm. In subfigures (a)-(d) The black outlined circles in the density matrices represent the ideal theoretical states, whereas the colored, solid circles represent the experimentally measured states. The trace fidelities of all states with the ideal ones are noted above each density matrix. As can be seen, the fidelity diminishes as a function of the runtime of the algorithm due to dephasing and relaxation of the qubit register. The experimental single-shot probabilities in subfigure (e) are shown along with the expected probabilities, which are calculated based on the readout matrix of our two-qubit system and the state tomographies after the final state of the algorithm.

7.4.2 Single Run Results

The experimental state tomographies discussed in the last section show that we are able to implement the Grover search algorithm with adequate fidelity using our two-qubit processor. However, the analysis of the two-qubit register by quantum state tomography at the end of the algorithm does not prove that we can achieve real quantum speed-up with our processor. For this, it is necessary to directly read out the state of the qubit register at the end of the algorithm *without* performing any kind of error correction afterwards. By looking at this “raw” outcome data and averaging it over many identical runs of the

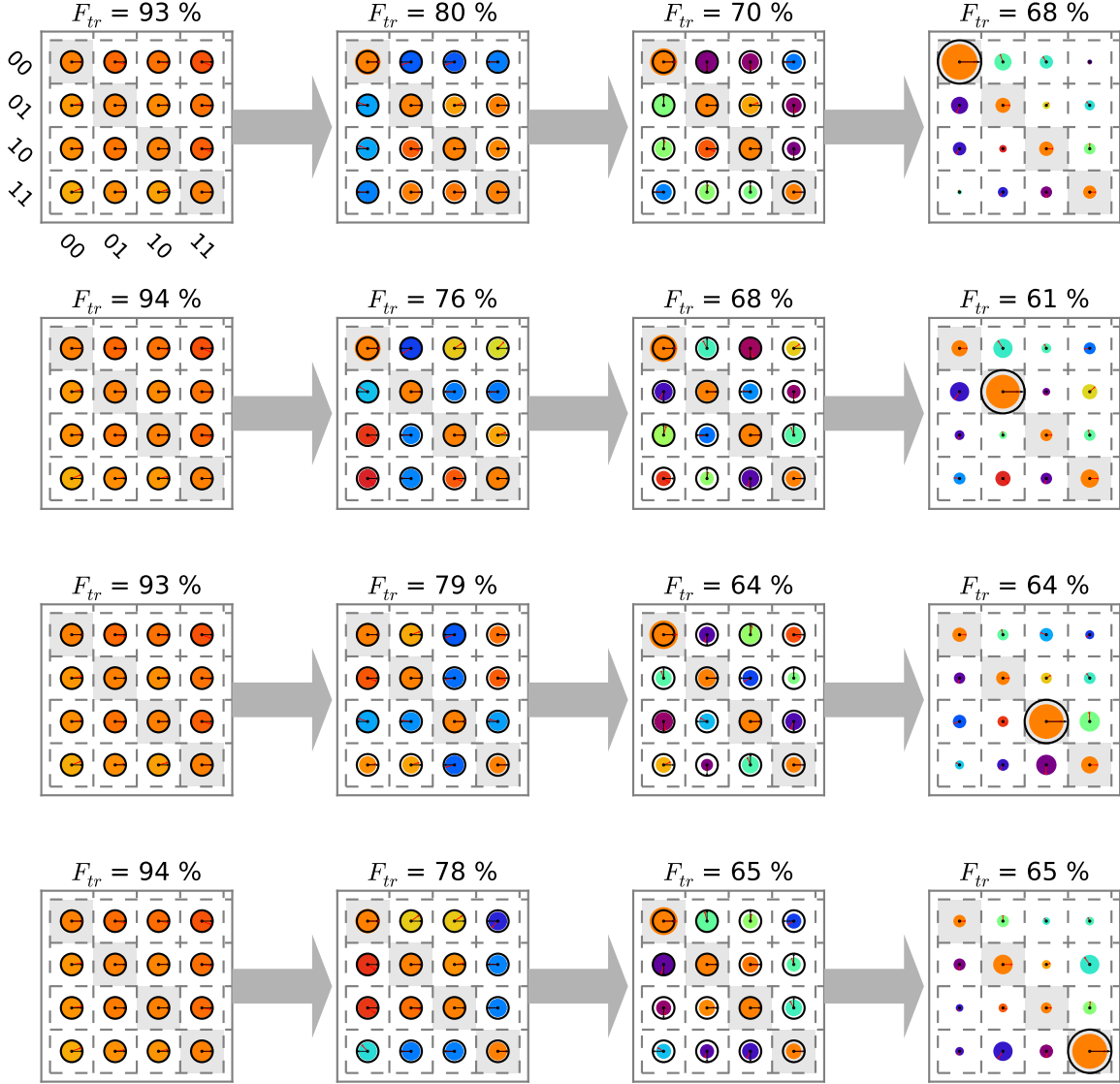


Figure 7.7: Quantum state tomographies at different steps of the Grover search algorithm and single-run outcome probabilities. The density matrices show the experimentally measured states in color and the theoretical states in black. For each state, the trace fidelity $F_{tr}(\rho_A, \rho_B) = \text{Tr}\{\rho_A \cdot \rho_B\}$ is shown above the density matrix.

processor we can then quantify the success rate and the fidelity of the algorithm we implemented. The results of such measurements that we performed for the four possible Oracle functions is shown in fig. 7.8. There, the different plots represent averaged outcome probabilities when measuring the state of the two-qubit register after performing the Grover algorithm, shown for all four possible Oracle functions. For comparision, we also show the expected outcome probabilities that are calculated based on the quantum state tomographies discussed above and the readout matrix of the two-qubit system. As can be seen, the agreement between the measured and calculated probabilities is quite good. The dashed line in all plots corresponds to the success probability of a classical

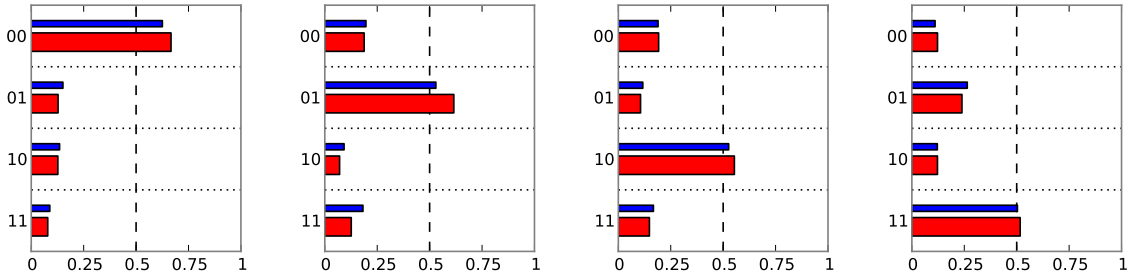


Figure 7.8: The single-run success probabilities of our implementation of the Grover search algorithm. Shown are the averaged probabilities for the four possible Oracle functions. The red bars correspond to measured values, the blue ones to expected probabilities calculated using the reconstructed density matrices after the final step of the algorithm and the measured two-qubit readout matrix. The dashed line indicates the average success probability of a classical query-and-guess algorithm for comparison.

“query-and-guess” algorithm, which is bound to 50 % and is therefore the benchmark for quantum speed-up in this system. As can be seen, our implementation of the Grover search algorithm outperforms a classical search algorithm for all four Oracle functions.

7.5 Algorithm Fidelity

We can define the average fidelity of the algorithm in a single run, which corresponds to the averaged success probabilities measured for all four Oracle functions and averaged over a large sample set. Table 7.1 shows these single-run probabilities along with the so-called *user fidelities*, which are given as

$$f_{ab} = p(|ab\rangle |ab) = \frac{p(ab| |ab\rangle)}{\sum_{uv} p(uv| |uv\rangle)} \quad (7.12)$$

and correspond to the probability of having obtained the correct answer given a certain outcome, averaged over all four possible Oracle functions. For all four, both the single-run and user fidelities are > 50%, hence providing a quantum speed-up in comparison with a classical query-and-guess algorithm.

$ab/ uv\rangle$	$ 00\rangle$	$ 01\rangle$	$ 10\rangle$	$ 11\rangle$	Σ	f_{ab}
00	0.666	0.192	0.188	0.122	1.168	57.0 %
01	0.127	0.554	0.071	0.122	0.874	63.4 %
10	0.128	0.106	0.615	0.239	1.088	56.5 %
11	0.079	0.148	0.126	0.517	0.870	59.4 %

Table 7.1: Conditional probabilities $p_{ab/|uv\rangle}$ and statistical fidelities f_{ab} for all possible outcomes ab , measured for our version of Grover’s algorithm.

7.6 Error Analysis

There are three kind of errors arising in our implementation of the Grover search algorithm which we will analyze in the following section. These errors are:

1. Deterministic, unitary gate errors arising in the algorithm
2. Stochastic errors introduced due to qubit decoherence during the runtime of the algorithm.
3. Readout errors due to qubit relaxation during the readout of the qubit state, insufficient coupling between the qubit and the readout or retrapping of the readout state during latching.

7.6.1 Gate Errors & Decoherence

Gate errors are unitary errors that arise due to misshaped or mistuned gate pulses. Usually the effect of these errors is combined with stochastic, non-unitary error sources arising due to qubit decoherence during the runtime of the algorithm. To quantify these errors we generate a model of our algorithm where we take into account both unitary as well as non-unitary error sources and perform numerical optimization of the error parameters to generate a quantitative model. We repeat this procedure for all four algorithm runs corresponding to the different Oracle functions.

Decoherence

Usually we can model decoherence processes in our algorithm either by integrating an effective master equation. For our error model, however, we chose to use a set of discrete decoherence operators that model amplitude (i.e. T_1) and phase damping (i.e. T_ϕ) processes. We can model the decoherence in our algorithm by applying these operators to the calculated quantum states after each individual step of the algorithm, taking into account the experimental runtime of the step. By this we can generate an error model incorporating the most relevant experimental decoherence processes without needing to numerically integrate a Lindblad equation, thereby greatly speeding up the parameter fitting.

The single-qubit operators describing amplitude-damping (i.e. energy relaxation) of the qubit state are given as (Michael A. Nielsen and Isaac L. Chuang, 2000)

$$E_1^{T_1} = \begin{pmatrix} 1 & 0 \\ 0 & \sqrt{1 - \gamma_{T_1}} \end{pmatrix} \quad E_2^{T_1} = \begin{pmatrix} 0 & \sqrt{\gamma_{T_1}} \\ 0 & 0 \end{pmatrix} \quad (7.13)$$

The phase-damaging (i.e. dephasing) operators can be written as

$$E_1^{T_{\phi 1}} = \begin{pmatrix} 1 & 0 \\ 0 & \sqrt{1 - \gamma_{\phi}} \end{pmatrix} \quad E_2^{T_{\phi 1}} = \begin{pmatrix} 0 & 0 \\ 0 & \sqrt{\gamma_{\phi}} \end{pmatrix} \quad (7.14)$$

Both operators are applied to ρ according to

$$\rho \rightarrow E_1 \rho E_1^\dagger + E_2 \rho E_2^\dagger \quad (7.15)$$

and result in a trace-preserving, non-unitary evolution of the quantum state of ρ . The decoherence factors γ in the operators can be calculated from the corresponding relaxation and dephasing rates as $\gamma_{T_{1,2}}(t) = 1 - \exp(-t\Gamma_{1,2})$ and $\gamma_{\phi_{1,2}} = 1 - \exp(-t\Gamma_{1,2}^{T_{\phi}}/2)$, where t is the time during which the state is exposed to the decoherence process.

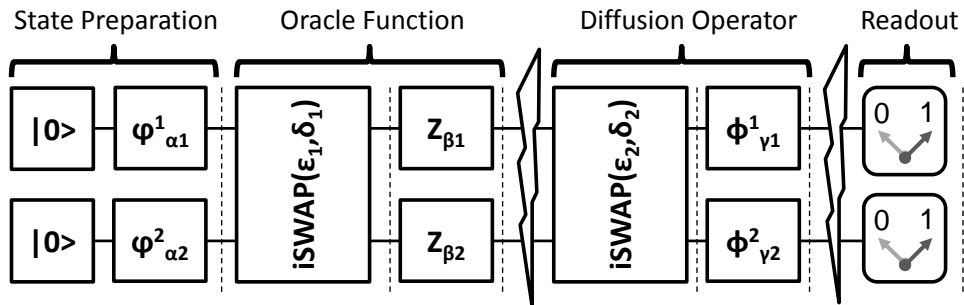


Figure 7.9: The error model we use to analyze the different gate and decoherence errors present when running the Grover search algorithm. The dotted lines indicate the points at which the quantum state has been measured by state tomography. Zigged arrows indicate the decoherence present in the system.

The full error model that we use to model the algorithm is shown in fig. 7.9. In this model, we take into account the following errors

- **Energy relaxation and phase decoherence:** We model energy relaxation and phase relaxation of our qubit by using the processes given in eqs. (7.13) and (7.14), applying the energy relaxation operator after each step of the algorithm, taking into account gate time of the performed operation.
- **Single-qubit gate errors:** We model rotation angle and rotation phase errors of our single-qubit X_α and Y_α gates by replacing them with operators of the form $X_\alpha \rightarrow \phi_{\alpha'} = \cos \phi X_{\alpha'} + \sin \phi Y_{\alpha'}$ and $Y_\alpha \rightarrow \varphi_{\alpha'} = \sin \varphi X_{\alpha'} + \cos \varphi Y_{\alpha'}$. For Z -type single-qubit operators we model only rotation angle errors by replacing $Z_\alpha \rightarrow Z_{\alpha'}$.
- **Two-qubit gate errors:** We model both detuning and gate-length errors of our $i\text{SWAP}$ 2-qubit gates.

The evolution operator of a detuned iSWAP operation is given as

$$i\text{SWAP}(t, \Delta) = \begin{pmatrix} 1 & 0 & 0 & 0 \\ 0 & \cos t g_e - i \frac{\Delta}{g_e} \sin t g_e & i \frac{g}{g_e} \sin t g_e & 0 \\ 0 & i \frac{g}{g_e} \sin t g_e & \cos t g_e + i \frac{\Delta}{g_e} \sin t g_e & 0 \\ 0 & 0 & 0 & 1 \end{pmatrix} \quad (7.16)$$

where $g_e = \sqrt{g^2 + \Delta^2}$ is the effective swap frequency at a qubit frequency detuning $f_{01}^1 - f_{01}^2 = 2\Delta$. Often it is practical to replace t and Δ with $\beta = t g_e$ and $\delta = \Delta/g$. Using this notation of the iSWAP gate and the definition of the single-qubit gates as discussed before, the full algorithm with gate errors can be written as (for right-multiplication)

$$\text{Grover} = \phi_{\gamma_1}^1 \otimes \phi_{\gamma_2}^2 \cdot i\text{SWAP}(\epsilon_2, \delta_2) \cdot Z_{\beta_1} \otimes Z_{\beta_2} \cdot i\text{SWAP}(\epsilon_1, \delta_1) \cdot \varphi_{\alpha_1}^1 \otimes \varphi_{\alpha_2}^2 \quad (7.17)$$

In addition, we add a dephasing and relaxation error after each step of the algorithm to simulate the decoherence during the executing. Numerical optimization is used to produce a fit of all the gate error parameters, which is shown in tab. 7.2. The qubit relaxation and dephasing times have been measured independently and are not part of the fit.

state	δ_1	δ_2	α_1	α_2	φ_1	φ_2	ϵ_1	β_1	β_2	ϵ_2	γ_1	γ_2	ϕ_1	ϕ_2
$ 00\rangle$	0.06	-0.06	-2.5	2.7	6.1	3.1	-7.3	-3.3	-4.1	7.5	29	9.3	0.66	-1.7
$ 01\rangle$	0.04	-0.3	-0.1	0.1	7.9	3.6	-11	-5.9	2.2	-6.9	28	-19	9	2
$ 10\rangle$	0.09	-0.2	-3.1	1.7	1	-2.5	-6.5	-15	-22	-7.5	-15	32	3.6	5.2
$ 11\rangle$	0.16	0.13	-6	3.9	2.2	0.9	-9.5	-20	-15	17	-12	-32	-7	-8.9

Table 7.2: Fitted error parameters for the measured density matrices, modeled according to the error model given in eq. (7.17). All angles are given in deg.

The results of the fitted error model are shown in tab. 7.2. As can be seen, the phase and gate-time errors for the first gates are comparatively small and grow bigger during the following steps of the algorithm. The phase errors are bigger for the states $|10\rangle$ and $|11\rangle$, as are the gate-length errors for the two iSWAP gates used in the algorithm.

Fig. 7.10 shows again the measured density matrices for our realization of the Grover search algorithm, this time overlaid with the numerically optimized error model according to eq. (7.17). As can be seen, our error model is able to capture most of the observed experimental errors and to reproduce to a very good accuracy the observed density matrices. The state fidelities according to eq. ?? between the measured density matrices and those of the fitted error model are shown above each density matrix.

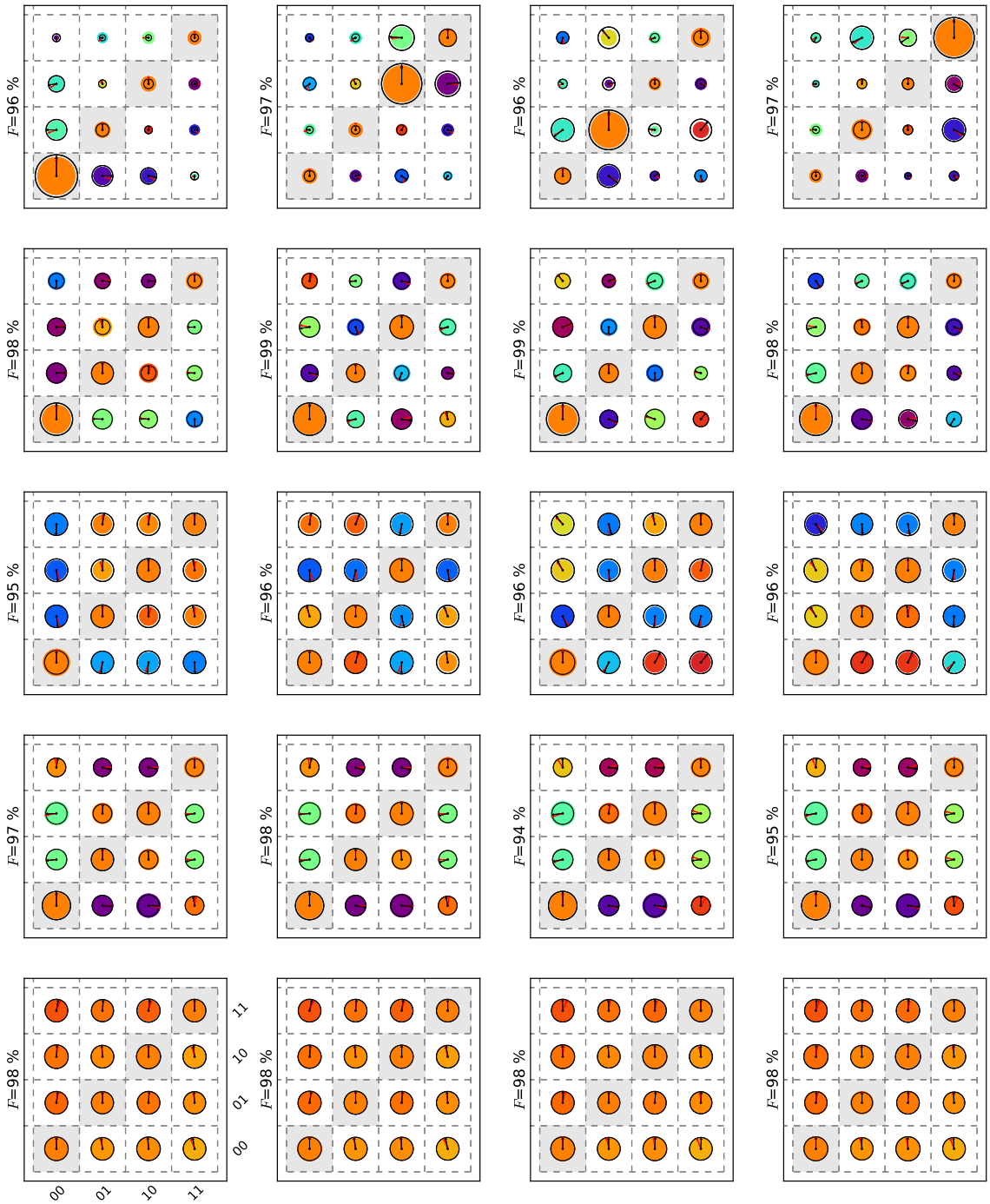


Figure 7.10: Quantum state tomographies at different steps of the Grover search algorithm and single-run outcome probabilities. The density matrices show the experimentally measured states in color and the theoretical states in black. For each state, the trace fidelity $F_{tr}(\rho_A, \rho_B) = \text{Tr}\{\rho_A \cdot \rho_B\}$ is shown above the density matrix.

Fidelity of the Oracle and diffusion operators

It is interesting to analyze the individual fidelity of the Oracle and diffusion operators that make up the Grover algorithm. For this, we compare the action of the ideal operators D' and R' with that of the experimentally implemented versions D'_e and R'_e , taking the measured quantum states before applying each of the operators as input. We take as the fidelity of each operator the average state fidelity of the measured output states as compared to the calculated ones, such that

$$F(D'_e) = F(D'\rho_{in}D'^\dagger, D'_e\rho_{in}D'^\dagger) \quad (7.18)$$

$$F(R'_e) = F(R'\rho_{in}R'^\dagger, R'_e\rho_{in}R'^\dagger) \quad (7.19)$$

where we also use the state fidelity according to eq. ???. By this method, we obtain the following fidelities for the two gate operations:

Operator / State	$ 00\rangle$	$ 01\rangle$	$ 10\rangle$	$ 11\rangle$	Average
D'	92.3	93.4	94.3	91.7	92.9
R'	94.5	93.6	88.5	87.7	91.1

Table 7.3: Measured fidelities of the quantum Oracle and diffusion operators used in the Grover search algorithm according to eqs. (7.18) and (7.19). All fidelities are given in percent.

7.6.2 Readout Errors

Another source of errors arises due to the imperfection of our qubit readout. Mostly, qubit relaxation during the readout process reduces the visibility of individual qubit states and introduces errors when reading out the qubit register in the final step of the algorithm. We can easily quantify those readout errors by using the readout matrix that was introduced in the last chapter. When running the Grover algorithm we use the $|1\rangle \rightarrow |2\rangle$ shelving method described in the last chapter to increase the readout contrast and thereby the algorithm fidelity. This technique reduces single-qubit readout errors but increases inter-qubit readout crosstalk. To quantify all single-qubit and inter-qubit readout errors, we first model the readout matrix R of the two-qubit system as a product $R = R_v \cdot R_{ct}$, where R_v is the so-called *visibility matrix* and R_{ct} a matrix describing the readout crosstalk. The visibility matrix can be written as the Kronecker product $R_v = R_v^1 \otimes R_v^2$ of the two single-qubit readout matrices, which have the form

$$R_v^{1,2} = \begin{pmatrix} p_{00}^{1,2} & 1 - p_{11}^{1,2} \\ 1 - p_{00}^{1,2} & p_{11}^{1,2} \end{pmatrix} \quad (7.20)$$

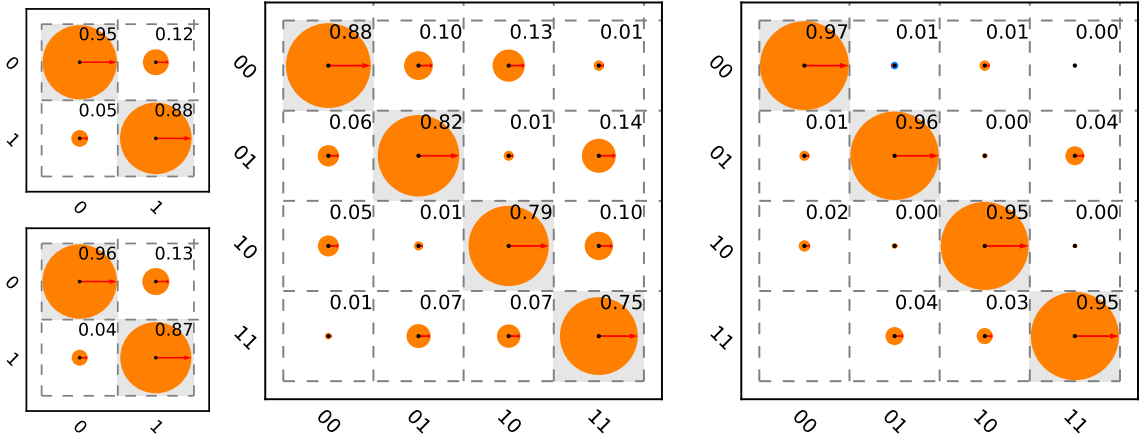


Figure 7.11: a.)The measured single-qubit readout matrices, showing the readout outcome probabilities as a function of the prepared state for both qubits. b.)The measured two-qubit readout matrix, showing again the detector outcome probabilities versus the prepared qubit states. c.) The crosstalk matrix, corresponding to the product of the two-qubit readout matrix and the Kronecker product of the single-qubit readout matrices. Note that the $|1\rangle \rightarrow |2\rangle$ shelving method is used for reading out the qubit state, which increases readout fidelity but also inter-qubit readout crosstalk.

Here, $p_{00}^{1,2}$ ($p_{11}^{1,2}$) corresponds to the probability to measure the value 0 (1) at the readout after having prepared the qubit in state $|0\rangle$ ($|1\rangle$). Usually, the full two-qubit readout matrix R and the single-qubit readout matrices $R_v^{1,2}$ are measured experimentally which allows us then to calculate the crosstalk matrix as $R_{ct} = R_v^{-1} \cdot R$. The three matrices measured in our experiment are shown in fig. 7.11. As can be seen, the single-qubit readout fidelities range between 87 - 96 % and the combined two-qubit readout fidelities between 75 - 85 %. Depending on the qubit state we also observe between 3-5 % inter-qubit readout crosstalk in our system.

Fig. 7.7e shows the single-run probabilities when running the Grover algorithm for the four different Oracle functions. In blue, the expected readout outcome probabilities, as calculated using the state tomography of the final states given in fig. 7.7d and the measured readout matrix of our system are shown along the measured readout outcome probabilities. The readout error model shows good quantitative agreement with the measured data, with deviations most probably due to parameter drifts occurred between the measurement of the quantum state tomography and the single-run experiment.

7.7 Conclusions

To summarize, we have shown that we can implement the Grover search algorithm with our quantum processor and achieve a single-run fidelity that is sufficient to demonstrate simple probabilistic quantum speed-up as compared to a classical, reversible search

algorithm. The error model formulated in this chapter is able to account for most of the observed imperfections and can explain the data we observed. The coherence times of our qubits does not permit the realization of more complex algorithm with this system, nevertheless it provides a proof-of-principle of our approach to build a superconducting quantum computer with individual-qubit single shot readout.

In the following chapter, we will discuss the extension of this approach to a system of four qubits and explain different strategies for scaling up such system to an even larger number of qubits.

Chapter 8

Designing a Scalable Architecture for Quantum Bits

8.1 Definition & Requirements

8.2 Qubit Design

8.2.1 Qubit Parameters

8.2.2 Qubit-Qubit Coupling

8.3 Readout Design

8.3.1 Readout Parameters

8.3.2 Qubit-Readout Coupling

8.4 Single-Qubit Manipulation

8.4.1 Error Analysis

8.5 Multi-Qubit Manipulation

8.5.1 Error Analysis

8.6 Implementing a Universal Set of Quantum Gates

8.7 Realizing A Four-Qubit Architecture

8.8 Scaling Up

Chapter 9

Conclusions & Perspective

9.1 Future Directions in Superconducting QC

9.1.1 3D Circuit Quantum Electrodynamics

9.1.2 Hybrid Quantum Systems

9.1.3 Quantum Error Correction & Feedback

Appendix A

Modeling of Multi-Qubit Systems

A.1 Analytical Approach

A.1.1 Multi-Qubit Hamiltonian

A.1.2 Energies and Eigenstates

A.2 Master Equation Approach

$$\frac{d\rho}{dt} = -\frac{i}{\hbar}[H, \rho] + \sum_j [2L_j \rho L_j^\dagger - \{L_j^\dagger L_j, \rho\}] \quad (\text{A.1})$$

A.2.1 Direct Integration

A.2.2 Monte Carlo Simulation

A.2.3 Speeding Up Simulations

Appendix B

Data Acquisition & Management

B.1 Data Acquisition Infrastructure

B.2 Data Management Requirements

B.3 PyView

B.3.1 Overview

B.3.2 Instrument Management

B.3.3 Data Acquisition

B.3.4 Data Management

B.3.5 Data Analysis

Appendix C

Design & Fabrication

C.1 Mask Design

C.2 Optical Lithography

C.3 Electron Beam Lithography

Bibliography

- Baur, M., Philipp, S., Bianchetti, R., Fink, J. M., Göppel, M., Steffen, L., Leek, P. J., Blais, A., and Wallraff, A. (2009). Measurement of Autler-Townes and mollow transitions in a strongly driven superconducting qubit. *Physical Review Letters*, 102(24):243602.
- Blais, A., Huang, R., Wallraff, A., Girvin, S. M., and Schoelkopf, R. J. (2004). Cavity quantum electrodynamics for superconducting electrical circuits: An architecture for quantum computation. *Physical Review A*, 69(6):062320.
- Chiorescu, I., Nakamura, Y., Harmans, C. J. P. M., and Mooij, J. E. (2003). Coherent quantum dynamics of a superconducting flux qubit. *Science*, 299(5614):1869–1871.
- Clarke, J., Cleland, A. N., Devoret, M. H., Esteve, D., and Martinis, J. M. (1988). Quantum mechanics of a macroscopic variable: The phase difference of a josephson junction. *Science*, 239(4843):992–997.
- Clauser, J. F., Horne, M. A., Shimony, A., and Holt, R. A. (1969). Proposed experiment to test local Hidden-Variable theories. *Physical Review Letters*, 23(15):880–884.
- Collin, E., Ithier, G., Aassime, A., Joyez, P., Vion, D., and Esteve, D. (2004). NMR-like control of a quantum bit superconducting circuit. *Physical Review Letters*, 93(15):157005.
- Cottet, A. (2002). *Implementation of a quantum bit in a superconducting circuit*. PhD thesis, Université Paris VI, Paris.
- Devoret, M. H., Martinis, J. M., and Clarke, J. (1985). Measurements of macroscopic quantum tunneling out of the Zero-Voltage state of a Current-Biased josephson junction. *Physical Review Letters*, 55(18):1908–1911.
- DiCarlo, L., Chow, J. M., Gambetta, J. M., Bishop, L. S., Johnson, B. R., Schuster, D. I., Majer, J., Blais, A., Frunzio, L., Girvin, S. M., and Schoelkopf, R. J. (2009). Demonstration of two-qubit algorithms with a superconducting quantum processor. *Nature*, 460(7252):240–244.

- DiCarlo, L., Reed, M. D., Sun, L., Johnson, B. R., Chow, J. M., Gambetta, J. M., Frunzio, L., Girvin, S. M., Devoret, M. H., and Schoelkopf, R. J. (2010). Preparation and measurement of three-qubit entanglement in a superconducting circuit. *Nature*, 467(7315):574–578.
- DiVincenzo, D. P. (2000). The physical implementation of quantum computation. *Fortschritte der Physik*, 48(9-11):771–783.
- Fedorov, A., Steffen, L., Baur, M., and Wallraff, A. (2011). Implementation of a toffoli gate with superconducting circuits. *arXiv:1108.3966*.
- Grover, L. K. (1997). Quantum mechanics helps in searching for a needle in a haystack. *Physical Review Letters*, 79(2):325–328.
- Grover, L. K. (2001). From schrödinger’s equation to the quantum search algorithm. *American Journal of Physics*, 69(7):769–777.
- Haroche, S. and Raimond, J. (2006). *Exploring the Quantum: Atoms, Cavities and Photons*. Oxford University Press.
- Johnson, B. R., Reed, M. D., Houck, A. A., Schuster, D. I., Bishop, L. S., Ginossar, E., Gambetta, J. M., DiCarlo, L., Frunzio, L., Girvin, S. M., and Schoelkopf, R. J. (2010). Quantum non-demolition detection of single microwave photons in a circuit. *Nature Physics*, 6(9):663–667.
- Koch, J., Yu, T. M., Gambetta, J., Houck, A. A., Schuster, D. I., Majer, J., Blais, A., Devoret, M. H., Girvin, S. M., and Schoelkopf, R. J. (2007). Charge-insensitive qubit design derived from the cooper pair box. *Physical Review A*, 76(4):042319.
- Lanyon, B. P., Hempel, C., Nigg, D., Müller, M., Gerritsma, R., Zähringer, F., Schindler, P., Barreiro, J. T., Rambach, M., Kirchmair, G., Hennrich, M., Zoller, P., Blatt, R., and Roos, C. F. (2011). Universal digital quantum simulation with trapped ions. *Science*, 334(6052):57–61.
- Lloyd, S. (1996). Universal quantum simulators. *Science*, 273(5278):1073–1078.
- Majer, J., Chow, J. M., Gambetta, J. M., Koch, J., Johnson, B. R., Schreier, J. A., Frunzio, L., Schuster, D. I., Houck, A. A., Wallraff, A., Blais, A., Devoret, M. H., Girvin, S. M., and Schoelkopf, R. J. (2007). Coupling superconducting qubits via a cavity bus. *Nature*, 449(7161):443–447.
- Mallet, F., Ong, F. R., Palacios-Laloy, A., Nguyen, F., Bertet, P., Vion, D., and Esteve, D. (2009). Single-shot qubit readout in circuit quantum electrodynamics. *Nat Phys*, 5(11):791–795.

- Martinis, J. M., Devoret, M. H., and Clarke, J. (1985). Energy-Level quantization in the Zero-Voltage state of a Current-Biased josephson junction. *Physical Review Letters*, 55(15):1543–1546.
- Martinis, J. M., Nam, S., Aumentado, J., and Urbina, C. (2002). Rabi oscillations in a large Josephson-Junction qubit. *Physical Review Letters*, 89(11):117901.
- Michael A. Nielsen and Isaac L. Chuang (2000). *Quantum Computation and Quantum Information*. Cambridge University Press.
- Mooij, J. E., Orlando, T. P., Levitov, L., Tian, L., van der Wal, C. H., and Lloyd, S. (1999). Josephson Persistent-Current qubit. *Science*, 285(5430):1036 –1039.
- Motzoi, F., Gambetta, J. M., Rebentrost, P., and Wilhelm, F. K. (2009). Simple pulses for elimination of leakage in weakly nonlinear qubits. *Physical Review Letters*, 103(11):110501.
- Nakamura, Y., Pashkin, Y. A., and Tsai, J. S. (1999). Coherent control of macroscopic quantum states in a single-Cooper-pair box. *Nature*, 398(6730):786–788.
- Paik, H., Schuster, D. I., Bishop, L. S., Kirchmair, G., Catelani, G., Sears, A. P., Johnson, B. R., Reagor, M. J., Frunzio, L., Glazman, L. I., Girvin, S. M., Devoret, M. H., and Schoelkopf, R. J. (2011). Observation of high coherence in josephson junction qubits measured in a Three-Dimensional circuit QED architecture. *Physical Review Letters*, 107(24):240501.
- Palacios-Laloy, A. (2010). *Superconducting qubit in a resonator: Test of the Leggett-Garg inequality and single-shot readout*. PhD thesis, Université Paris VI, Paris.
- Reed, M. D., DiCarlo, L., Nigg, S. E., Sun, L., Frunzio, L., Girvin, S. M., and Schoelkopf, R. J. (2011). Realization of Three-Qubit quantum error correction with superconducting circuits. *arXiv:1109.4948*.
- Schuster, D. I., Houck, A. A., Schreier, J. A., Wallraff, A., Gambetta, J. M., Blais, A., Frunzio, L., Majer, J., Johnson, B., Devoret, M. H., Girvin, S. M., and Schoelkopf, R. J. (2007). Resolving photon number states in a superconducting circuit. *Nature*, 445(7127):515–518.
- Siddiqi, I., Vijay, R., Metcalfe, M., Boaknin, E., Frunzio, L., Schoelkopf, R. J., and Devoret, M. H. (2006). Dispersive measurements of superconducting qubit coherence with a fast latching readout. *Physical Review B*, 73(5):054510.

- Siddiqi, I., Vijay, R., Pierre, F., Wilson, C. M., Metcalfe, M., Rigetti, C., Frunzio, L., and Devoret, M. H. (2004). RF-Driven josephson bifurcation amplifier for quantum measurement. *Physical Review Letters*, 93(20):207002.
- Vijay, R., Devoret, M. H., and Siddiqi, I. (2009). Invited review article: The josephson bifurcation amplifier. *Review of Scientific Instruments*, 80(11):111101–111101–17.
- Vijay, R., Slichter, D. H., and Siddiqi, I. (2011). Observation of quantum jumps in a superconducting artificial atom. *Physical Review Letters*, 106(11):110502.
- Vion, D., Aassime, A., Cottet, A., Joyez, P., Pothier, H., Urbina, C., Esteve, D., and Devoret, M. H. (2002). Manipulating the quantum state of an electrical circuit. *Science*, 296(5569):886 –889.
- Wallraff, A., Schuster, D. I., Blais, A., Frunzio, L., Huang, R.-S., Majer, J., Kumar, S., Girvin, S. M., and Schoelkopf, R. J. (2004). Strong coupling of a single photon to a superconducting qubit using circuit quantum electrodynamics. *Nature*, 431(7005):162–167.